Remote Sensing of Environment 267 (2021) 112718

Contents lists available at ScienceDirect

Remote Sensing of Environment

journal homepage: www.elsevier.com/locate/rse

Spatio-spectral deconvolution for high resolution spectral imaging with an application to the estimation of sun-induced fluorescence

Hanno Scharr [a,b,*], Patrick Rademske [a], Luis Alonso [c], Sergio Cogliati [d], Uwe Rascher [a]

[a] Institute of Bio- and Geosciences (IBG), IBG-2: Plant Sciences, Forschungszentrum Jülich GmbH, D-52425 Jülich, Germany
[b] Institute for Advanced Simulation (IAS), IAS-8: Data Analytics and Machine Learning, Forschungszentrum Jülich GmbH, D-52425 Jülich, Germany
[c] Image Processing Laboratory, University of Valencia, Valencia, Spain
[d] Remote Sensing of Environmental Dynamics Lab., DISAT, University of Milano-Bicocca, P.zza della Scienza 1, 20126 Milano, Italy

ARTICLE INFO

Edited by Jing M. Chen

Keywords:
Sun-induced fluorescence (SIF)
Deconvolution of measured PSF and signal
Calibration simulation
Quantitative analysis
O_2A
O_2B
Imaging spectrometer

ABSTRACT

We propose a signal deconvolution procedure for imaging spectrometer data, where a measured point spread function (PSF) is deconvolved itself before being used for deconvolution of the signal. We evaluate the effectiveness of our procedure for improvement of the spatio-spectral signal, as well as our target application, i.e. estimation of sun-induced fluorescence (SIF). Imaging spectrometers are well established instruments for remote sensing. When used for scientific purposes these instruments are usually calibrated on a regular basis. In our case the point spread function of the optics is measured in an elaborate procedure with a tunable monochromator point light source. PSFs are measured at different pixel positions of the imaging sensor, i.e. at different spatio-spectral locations, and averaged in order to get an as accurate PSF as possible. We investigate error sources in this calibration process by simulating the procedure in silico. Averaging as well as the spectral and spatial width of the point source introduce some smoothness in the measured PSF. We propose corrective measures, i.e. deconvolution of the PSF itself and median instead of mean averaging, leading to a set of sharper PSFs. We test the performance of these PSFs in deconvolving simulated as well as real hyperspectral images. For deconvolution we test a set of well-known, off the shelf deconvolution algorithms. Quantitatively in terms of PSNR (Peak Signal to Noise Ratio) a combination of Wiener filtering and sharpened PSFs yields strongest improvements, while using Wiener filtering with non-sharpened PSFs even deteriorates the signal. Comparing deconvolution results of the simulated data with results of real data reveals, that visually very similar effects can be observed. This well supports the assumption, that our findings are also valid for real spatio-spectral data. Surprisingly, the choice of PSF, sharpened or not, is of little effect for SIF estimation with the iFLD algorithm in the O_2A band. Quantitatively we find that deconvolution reduces the overall error of SIF by a factor of 3.8, when using Wiener filtering instead of the currently used 1 iteration of vanCittert's method. For SIF estimation in the O_2B band we observe a totally different behavior, where all deconvolution methods yield unreliable results with mostly well above 200% relative error and high standard deviations. In the discussion we can only speculate on possible reasons for this unreliability. As conclusion we therefore propose to use the O_2A band for SIF estimation together with classic Wiener filtering for deconvolution of spatio-spectral data.

1. Introduction

Photosynthetic light conversion constitutes the main biochemical reaction that ultimately fuels all life on earth by converting the energy of the solar radiation into biochemically usable energy compounds. During the process of photosynthesis, plants absorb solar radiation in their photosynthetic pigments, stabilize this energy in the electron transport chain of photosynthetic light reaction, and finally use the energy for carbon fixation. As a side product of photosynthesis a small fraction of the absorbed energy is re-emitted as a weak red fluorescence light (the so-called chlorophyll fluorescence), which changes intensity in relation to the efficiency of the photosynthetic processes.

* Corresponding author at: Institute for Advanced Simulation (IAS), IAS-8: Data Analytics and Machine Learning, Forschungszentrum Jülich GmbH, D-52425 Jülich, Germany.
E-mail addresses: h.scharr@fz-juelich.de (H. Scharr), p.rademske@fz-juelich.de (P. Rademske), luis.alonso@uv.es (L. Alonso), sergio.cogliati@unimib.it (S. Cogliati), u.rascher@fz-juelich.de (U. Rascher).

https://doi.org/10.1016/j.rse.2021.112718
Received 7 March 2021; Received in revised form 13 September 2021; Accepted 23 September 2021
Available online 6 October 2021

The close link between the functional status of photosynthesis and the intensity of the chlorophyll fluorescence signal had fostered the development of various instruments and measurement approaches that exploit the chlorophyll fluorescence signal as a non-invasive reporter of the functional status of photosynthesis (Murchie et al., 2018). Most of the established fluorescence measurement protocols are active approaches, which work on the single leaf level and where the fluorescence signal is stimulated by specific measurement lights. However, in recent years the measurements of sun-induced fluorescence (SIF) have gained wide scientific interest (see e.g. (Mohammed et al., 2019) for a recent review), which was lately stimulated by the selection of the FLEX satellite mission by the European Space Agency (Drusch et al., 2017).

Even though SIF is not easy to interpret physiologically, SIF opens the unique possibility to be measured passively also from remote sensing platforms (see e.g. (Damm et al., 2014; Guanter et al., 2012; Köhler et al., 2018)). Thus, by exploiting SIF we may have the unique possibility to quantify actual rates of photosynthesis on the large, i.e. ecosystem and global scale and to quantify actual rates of photosynthesis from remote sensing platforms (Mohammed et al., 2019).

Sun-induced fluorescence is a rather weak signal that in practice is masked by much stronger intensities of reflected light. Thus, SIF measurements often exploit solar and telluric absorption features, where the emitted fluorescence signal is relatively larger than the reflected background light (Meroni et al., 2009). There are several solar and telluric absorption features in the spectral window where chlorophyll fluorescence is emitted and most commonly the atmospheric oxygen absorption features around the oxygen absorption band A and B (O_2A and O_2B band) are used to retrieve SIF. The O_2A band at 761 nm is ~2 nm wide and thus SIF can most easily be retrieved using this absorption feature (Damm et al., 2014). However, the O_2B band as well as small band solar absorption lines (so-called Fraunhofer lines) have also been used to retrieve SIF (Guanter et al., 2012; Köhler et al., 2018). For retrieving SIF in the absorption features the Fraunhofer Line Discrimination (FLD) method can be used, which in the strict sense only requires one measurement outside and one measurement inside the absorption feature to quantify fluorescence (Plascyk and Gabriel (1975), Moya and Cerovic (2004), cmp. Section 2.6).

Nowadays spectrometers with high spectral resolution are used for SIF measurements, which can be either point spectrometers or imaging systems. Push broom line scanning spectrometers record spatio-spectral signals by means of a bi-dimensional sensor where the spatial information is collected in one dimension while spectral information is captured along the other dimension.

Ideally, a monochromatic point light source should produce a single pixel response. In real systems this is not the case, and the resulting signal spreads across the sensor matrix according to the Point Spread Function (PSF) (Siegmann et al., 2019; Jähne, 2005; Jähne et al., 1999), an ubiquitous point of consideration in remote sensing (see e.g. McGillem et al. (1983), Huang et al. (2002), Peng et al. (2015), Waldner et al. (2018), Wang et al. (2020a,b)). For SIF retrievals from airborne and satellite platforms a detailed characterization of the PSF of a measuring system, including the degree of straylight is essential to account for instrument and atmospheric effect during signal acquisition (Barnes et al., 2010; Sabater et al., 2018). Also for dedicated SIF imaging spectrometers the optical characterization includes a description of the point spread characteristics of the system (Siegmann et al., 2019; Paynter et al., 2020).

Point-spead characteristcs and stay light most severely affect pixels with contrasting values in neighboring pixels, which in practice occurs at the absorption features, which are used for SIF retrievals, at narrow emission peaks, or at objects that have greatly different brightness at edges. In these cases some energy from a pixel with, high signal in a band of one surface can be transferred to a neighboring pixel and even very weak relative contributions in the PSF, can result in a noticeable effect at the weakly illuminated pixel. This effect is an inherent challenge for SIF retrievals, where the signal is extracted across spatially sharp absorption features (influence of the spectral effect of the PSF) and where edges between bright and dark surfaces shall be resolved (e.g. bright background vs. 'dark' vegetation reflectance with a superimposed fluorescence signal; influence of the spatial effect of the PSF).

Deconvolution is a well-known counter measure to the PSF effect (Wiener, 1942; Lucy, 1974; Richardson, 1972; Jähne, 2005). Even though well understood and theoretically well-founded, deconvolution is only an optional step in the currently established processing pipeline for HyPlant (Siegmann et al., 2019). There, only one iteration of van Cittert's method (Jähne, 2005) (see also Eqs. (6) and (7)) is recommended as more iterations deteriorate results. In experiments and discussions we use one iteration of van Cittert's method as baseline. Stronger acting deconvolution methods like Wiener filtering (Wiener, 1942) are not considered by Siegmann et al. (2019), even though Wiener filtering should optimally reconstruct the signal and therefore yield better results. In this paper, we investigate why stronger deconvolution with the PSF known from specific calibration measurements leads to undesirable results and propose a simple but effective sharpening of the measured PSF before applying strong deconvolution.

This work presents a quantification of PSF effects through a theoretical analysis of the impact of the PSF on push-broom spectrometers. A correction by means of a strong deconvolution process is proposed and its quantitative effect investigated on synthetic data. To this end realistic high-resolution radiance and SIF spectra were simulated in silico using state-of-the art radiative transfer models for plant canopies and atmosphere. Synthetic spectral images with the same characteristics as real spectral images from the HyPlant airborne hyperspectral imager (Rascher et al., 2015; Siegmann et al., 2019) were composed from the simulated spectra. They allow a quantitative evaluation of the impact of the PSF and the possible deconvolution on SIF retrievals from real world spectrometers. Experiments reveal that the signal quality of the spectral images improves strongly when using our proposed deconvolution method compared to the baseline from Siegmann et al. (2019) (Peak Signal to Noise Ratio (PSNR) increases from 36.7 to 40.3). The positive effect is even stronger for SIF estimates, where the mean squared error drops by a factor 3.8 and thus strongly improves reliability of SIF measurements. Qualitative comparisons between effects of different deconvolution approaches on synthetic data versus real HyPlant data indicate the validity of the presented findings also for real data.

2. Materials and methods

In our experiments we use real and synthetic hyperspectral imaging data, as well as measured and simulated calibration data to derive the sensors point spread function and use it for deconvolution.

The real data stems from an airborne imaging spectrometer HyPlant, more specifically from the so-called FLUO module of the HyPlant sensor (Rascher et al. (2015), Siegmann et al. (2019), see also Section 2.2). In the following, we discuss image formation in the light of its special properties (Section 2.2). We derive, how its PSF can be estimated from calibration data (Section 2.4), and how noise and therefore the signal-to-noise ratio can be estimated (Section 2.3). These are needed as input to well-known deconvolution algorithms, which we also briefly discuss in Section 2.1. In Section 2.5 we describe, how synthetic image are simulated, based on synthetic calibration data, allowing quantitative experiments later in Section 3. We briefly introduce sun induced fluorescence (SIF) retrieval (Section 2.6), as we use a retrieval of SIF to investigate the effect of deconvolution on this small signal component. Finally, a description of error measures used in Experiments is given in Section 2.7. Flowcharts in Fig. 1 give overview of components and their interaction in the workflows for (i) PSF calibration (cmp. Fig. 1, bottom), as well as (ii) the overall processing including deconvolution and subsequent SIF estimation (cmp. Fig. 1, top). There we also indicate in which sections the respective descriptions are to be found.

Before going into imaging details, we discuss the different deconvolution algorithms used in this study.

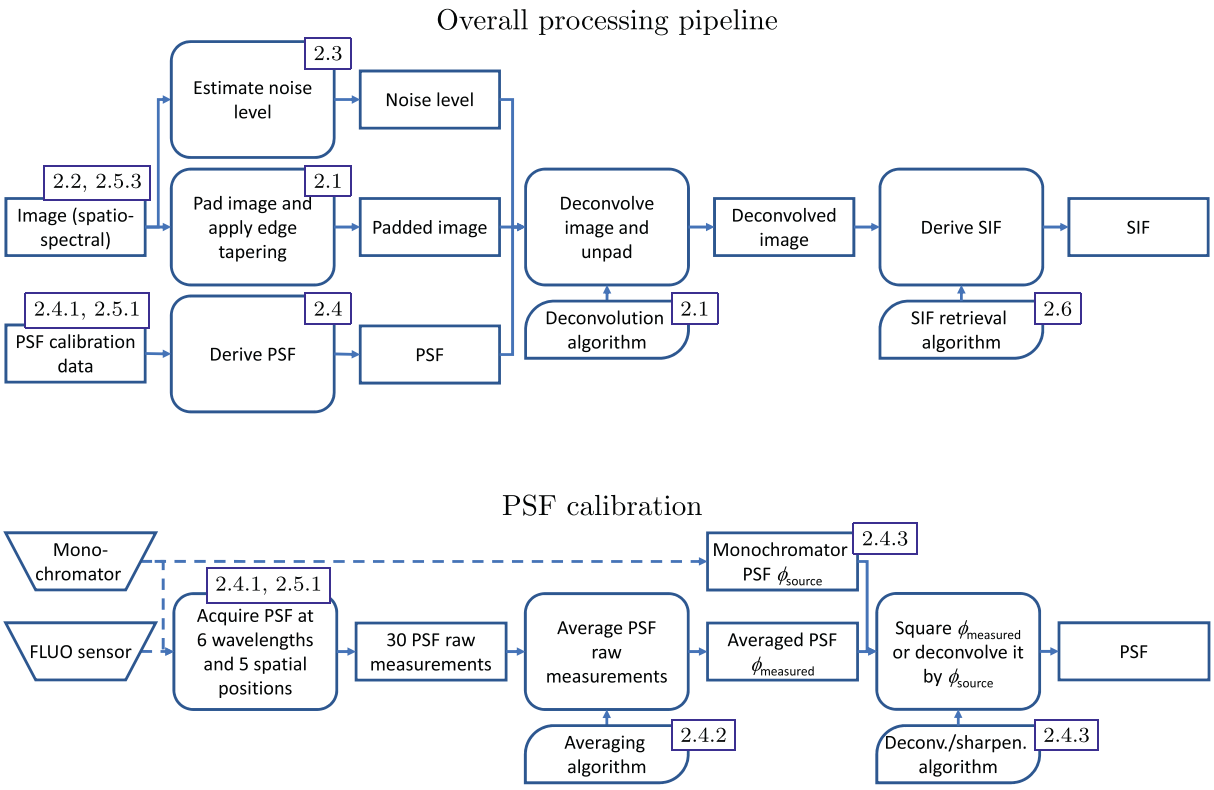

Fig. 1. Flowcharts. Boxes depict data, rounded off boxes are processing steps, and boxes rounded off at top left and bottom right are algorithms we focus on in this article, trapezoids are physical objects. Dashed arrows indicate application or properties of physical objects, solid arrows show input/output relations. Numbers indicate the sections, where to find respective descriptions in the text. Top: Overall processing pipeline for deconvolution and subsequent SIF estimation. Bottom: PSF derivation from calibration data, i.e. a zoom-in in the above box 'Derive PSF'.

2.1. Deconvolution algorithms

Signal deconvolution is a well-explored problem and a wide selection of deconvolution algorithms is available in textbooks (Jähne, 2005; Gonzalez and Woods, 1992) and image processing toolboxes (MathWorks, Inc., 1994; van der Walt et al., 2014). For our experiments, we used the Matlab image processing toolbox (MathWorks, Inc., 1994). One distinguishes between 'blind' and 'non-blind' algorithms, where 'non-blind' algorithms need an exactly characterized PSF as input, and 'blind' deconvolutions can update the initial PSF. The core idea of deconvolution algorithms is to undo the convolution of the signal I with the PSF φ. According to the convolution theorem of Fourier transform (see e.g. Jähne (2005)),

$$\varphi * I = \mathcal{F}^{-1}(\widehat{\varphi}\cdot\widehat{I}) \tag{1}$$

convolution * of φ and I in image domain is equivalent to point-wise multiplication $\cdot$ of the transfer functions $\widehat{\varphi} = \mathcal{F}(\varphi)$ and $\widehat{I} = \mathcal{F}(I)$, where $\mathcal{F}$ denotes Fourier transform and $\mathcal{F}^{-1}$ its inverse. Let us denote the measured signal or image by I_0. According to the convolution theorem, without noise and when $\widehat{\varphi} \neq 0$ everywhere, deconvolution is simply pointwise division by $\widehat{\varphi}$ of I_0 in Fourier domain $I_{\text{deconv}} = \mathcal{F}^{-1}(\widehat{\varphi}^{-1}\cdot\widehat{I}_0)$. As φ typically is a damping function with $|\widehat{\varphi}| < 1$ almost everywhere, division by $\widehat{\varphi}$ means signal amplification. Consequently, noise is also amplified when present in the signal. Methods implemented in Fourier domain thus often distinguish between regions with low noise (SNR < 1), where division by $\widehat{\varphi}$ is applied, and regions with high noise (SNR > 1), where it is not applied, or the signal is even further damped. Adequate noise handling is therefore essential to deconvolution methods and our studies (cmp. also Section 2.3).

In our experiments we investigated the performance of five deconvolution methods:

- Wiener filtering (Wiener (1942), Gonzalez and Woods (1992), abbreviated *deconvwnr*): The Wiener filter is designed to minimize the expected mean square error between the measured noisy signal I_{measured} and its reconstruction I_{deconv}, when SNR and PSF φ are known. This is achieved by

$$I_{\text{deconv}} = \mathcal{F}^{-1}\left(\frac{\widehat{\varphi}^*}{\widehat{\varphi}\cdot\widehat{\varphi}^* + \text{SNR}^{-1}}\cdot\widehat{I}_0\right) \tag{2}$$

  where * denotes complex conjugation. From the equation we see, that for high SNR Wiener filtering implements pointwise division by $\widehat{\varphi}$ and for low SNR the signal is damped.
- Regularized deconvolution (MathWorks Inc. (2021), Gonzalez and Woods (1992), abbreviated *deconvreg*): This method is similar to Wiener filtering, however, the regularization wrt. SNR is implemented differently:

$$I_{\text{deconv}} = \mathcal{F}^{-1}\left(\frac{\widehat{\varphi}^*}{\widehat{\varphi}\cdot\widehat{\varphi}^* + \lambda\widehat{L}\cdot\widehat{L}^*}\cdot\widehat{I}_0\right) \tag{3}$$

  where L is a Laplacian operator and λ a parameter determined by minimization such that the power of the deconvolution residuals near equals the noise power.
- The Lucy-Richardson algorithm with 7 or 12 iterations (Richardson (1972), Lucy (1974), Biggs (1997), Hanisch et al. (1997), abbreviated *LucyRichards7* and *LucyRichards12*): Here $I_{\text{deconv}} = I_n$ is the output I_n of an iterative scheme after n iterations:

$$I_{i+1} = (\varphi^{\mathrm{T}} * \frac{I_0}{\varphi * I_i})\cdot I_i \tag{4}$$

  with I_0 being the measured signal as defined above and where φ^{T} is a mirrored version of φ (cmp. Fish et al. (1995, Eq. 3)).

- A blind version of the Lucy-Richardson deconvolution scheme (MathWorks Inc., 2021; Fish et al., 1995): Here the above Lucy-Richardson iteration Eq. (4) updating the image is alternated with the same scheme applied to the PSF φ

$$\varphi_{i+1} = (I_i^{\mathrm{T}} * \frac{I_0}{\varphi_i * I_i}) \cdot \varphi_i \tag{5}$$

  where $\varphi_0 = \varphi$ and the updated PSF φ_{i+1} is used for updates of the image in Eq. (4).
- The non-blind vanCittert iterative update scheme with 1 or 3 iterations (Jähne (2005), abbreviated *vanCittert1* and *vanCittert3*): A discrete kernel $K = \delta - \varphi$ is defined, where δ is the identity operator of convolution, i.e. 1 at the origin and 0 else. This kernel is iteratively applied to the increment ΔI of image I:

$$(\Delta I)_{i+1} = K * (\Delta I)_i \tag{6}$$

$$I_{i+1} = I_i + (\Delta I)_{i+1} \tag{7}$$

  with $(\Delta I)_0 = I_0$.

In the practical handling vanCittert, Lucy-Richardson and blind deconvolution have the advantage that one does not need to provide a noise level, but an easier to understand iteration number.

All above algorithms require proper handling of image borders. Especially algorithms based on Fast Fourier Transform (FFT, (Heideman et al., 1984)), e.g. Wiener filtering or regularized deconvolution, would suffer from ringing artifacts without it and sophisticated boarder handling solutions exist (Skilling and Gull, 1985; Reeves, 2005; Simões et al., 2016). We use the widely adopted edge tapering (Skilling and Gull, 1985; MathWorks Inc, 2021) together with periodic padding, such that the original image region is unaffected by tapering.

Recent deconvolution solutions (see e.g. Kruse et al. (2017), Wang et al. (2019), Ren et al. (2020)) address imaging artifacts like camera shake or motion blur, where PSFs are complicated and not well peaked. In such situations, machine-learning based algorithms dramatically outperform the above described well established simpler deconvolution algorithms. This increased performance comes at a cost, as such algorithms contain sophisticated regularization terms which need to be adapted to or learned from training data. These regularization terms then formulate prior knowledge on the training data, which is good, when the measured data behaves like the training data, but introduce an unwanted and hard to control bias, when measured data differs from the training set. In the current study, we want to use prior knowledge on the signal as scarcely as possible, in order to avoid regularization bias; and at the same time use the available high-precision calibration data as much as possible.

2.2. Image formation and data format

The FLUO module of HyPlant is an imaging spectrometer designed for push-broom operation. It is commercially available under the name AisaIBIS (SPECIM, 2021) and described in more detail by Rascher et al. (2015), Siegmann et al. (2019). It features a spectral resolution of 2048 pixels over the range of approx. 670 nm to 780 nm and thus a spectral pixel width of approx. 0.054 nm/pixel. The sensor has 1536 pixels in the spatial dimension. The usual operation mode is 2×4-binning, i.e. the sensor then acquires 1024×384 pixel spatio-spectral images, usually also called 'lines', with 1024 spectral bands at 384 spatial positions.

The real data we work with in our experiments below stems from a measurement campaign in 2016 (European Space Agency & Forschungszentrum Jülich, 2016). It contains 301 spatio-spectral images, thus is a 3-dimensional data block of 1024×384×301, which we call $I_{\mathrm{real}}(\lambda, x, t)$. Here λ is the spectral wavelength, x is the spatial position on the sensor, and t the time in the image sequence, acting as second spatial coordinate, as the sensor is operated in push-broom fashion.

Collapsing the spectral dimension of this 3d block into suitable false colors yields therefore 2d spatial images like shown e.g. in Fig. 2, left. Each spatial pixel contains a spectrum, like the ones shown in Fig. 2, right.

In the following, for simplicity, if not stated differently, we call the signal delivered by the sensor a *2d image* or just *image*, even though it is a spectrally resolved spatial line. The spatio-spectral image is formed by the incoming light entering through a slit and being then defracted in the spectral direction by a grading, before hitting a 2d imaging sCMOS chip (Rascher et al., 2015).

As any real optical system (cmp. e.g. (Jähne et al., 1999; Jähne, 2005)), the sensor does not produce a perfectly sharp image, i.e. when a true spatial-spectral point source hits the sensor, the image does not just show a single illuminated pixel on black background, but spreads the peak over a small region on the sensor. The spatial response is usually called Point Spread Function (PSF) and the spectral response Instrument Spectral Response Function (ISRF) (Beirle et al., 2017; Jähne et al., 1999). In the following, for simplicity, we call the 2d combination of PSF and ISRF, a *spatial-spectral PSF* or just *PSF*.

Mathematically, image acquisition is modelled by several signal components. The incoming light is smoothed by being convolved with the PSF of the optical system. The light sensitive area of each pixel collects the incoming light, again convolving the so far spatially and spectrally continuous light signal by the pixel sensitivity function (typically assumed to be a square). Each pixel converts the incoming photons into an electric signal represented as a single number, i.e. the pixel intensity. The process performed by the pixels is usually called *sampling*. The pixel intensity contains noise stemming from the randomness of the number of photons hitting the sensor, called *shot* or *photon noise*, being Poisson distributed. The intensity is then discretized to a 16-bit representation, adding so called *quantization noise*, being uniformly distributed. Electronic components may add further noise, but for a high-end imaging spectrometer, where light is not only spatially distributed, but in addition also fragmented to different wavebands, the physically unavoidable photon noise is dominating (see e.g. Jähne et al. (1999)).

Formation of a real image I_{real} can thus in essence be summarized as

$$I_{\mathrm{real}}(\lambda, x, t) = \varphi(\lambda, x) * L(\lambda, x, t) + n(\varphi * L) \tag{8}$$

where we omit the quantization and sampling steps for readability. We denote convolution by *. Noise n mainly depends on the radiance L as described above. Derivation of PSF φ from calibration data is described in Section 2.4 and estimation of the noise level next in Section 2.3.

2.3. Noise estimation

Some of the above deconvolution algorithms, i.e. Wiener filtering and regularized deconvolution, need to be informed about the noise level in the image or the signal-to-noise ratio. Noise-level estimation for general images from unknown sources can be quite involved (see e.g. Liu et al., 2013). Considering noise appropriately is highly important as it is a limiting factor for deconvolution. Low noise makes deconvolution trivial, as it can then be performed by pointwise division of the signal by the transfer function of the PSF in Fourier domain (see Section 2.1 and Eq. (1)). High noise, however, can make deconvolution impossible. Working with the correct noise level is therefore key to this study. In our application of high-resolution spatio-spectral remote sensing images, there are two simple options available to derive the appropriate noise level.

One is to take the signal-amplitude dependent noise level derived in a radiometric calibration step, assuming that shot-noise is dominating. Radiometric calibration is performed by acquiring data while the sensor looks into a homogeneous, calibrated light source with continuously adjustable intensity; in our case an integrating sphere. The light source allowed to tune intensity from below detectable to sensor saturation (we

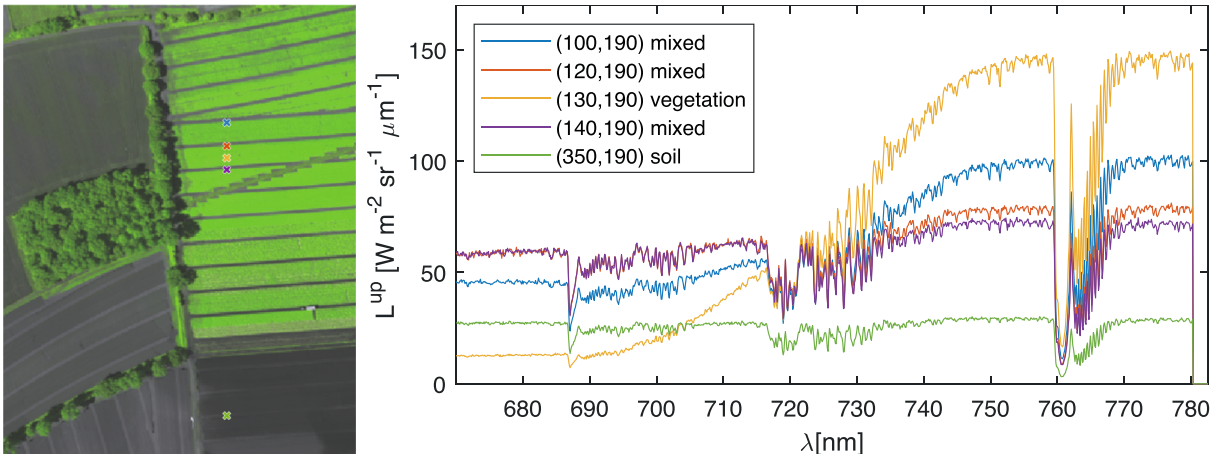

Fig. 2. Spatial-spectral real images. Left: Spatial component (384×301 pix) of real data I_{real} in pseudo colors(For interpretation of the references to color in this figure legend, the reader is referred to the web version of this article.), where vegetation is green and soil is gray. Flight direction is to the right, spatial direction of the sensor vertical. Colored crosses indicate spatial positions of the spectra on the right. Right: Five spectra from I_{real}. Legend gives their spatial pixel position in the left image.

selected 100 steps), where for each intensity 100 images where taken. Noise is then estimated as variation around the per pixel mean. For the FLUO module of HyPlant, the variance of this noise approximately increases linearly with 0.5 times pixel intensities.

The other is to estimate noise from the current spatio-spectral image. This is what we do in our experiments, below. We perform this noise estimation in Fourier domain. There, shot noise is uniformly distributed over the whole domain, however, the expected signal is not. It is concentrated around the Fourier domain origin and strongly decays towards higher Fourier frequencies. Inspecting the 2d Fourier signal one observes a plateau at highest frequencies with a mean value being representative for the noise level. We estimate this mean value simply by averaging over the region of highest frequencies. To do so, we select the top quarter of frequencies in each dimension, as we observed that it consistently is completely dominated by noise.

2.4. Derivation of the PSF

In order to reveal the PSF of the FLUO module,a set of individual PSF measurements at 30 different spatio-spectral sensor locations has been acquired, as detailed below. From this raw data several processing steps need to be taken into account in order to get a reliable estimate of the true underlying PSF.

2.4.1. Calibration measurements

The PSF of the FLUO module has been characterized using a Lot-Oriel monochromator (MSH-300 (Quantum Design Europe, 2021)), i.e. a spectral point source with 0.14 nm bandwidth, combined with spatial subpixel accurate focusing with unknown spatial PSF φ_{source}. Compared to the 0.054 nm spectral sampling of the FLUO module, the point source is about 2.5 pixel wide and thus cannot be considered to be a perfect point. Consequently the measured spatial-spectral PSF $\varphi_{\text{measured}}$ of FLUO may need to be considered as a convolution of the true FLUO PSF φ_{true} and the source's PSF φ_{source}.

PSF measurements were performed at six different wavelengths and five spatial positions on the sensor, i.e. 30 PSF instances overall. Visually inspecting the measurements revealed well noticeable asymmetries of the PSF peaks within their direct neighborhoods, i.e. their central 3×3 pixel region, respectively for each peak. We conclude that the spatial-spectral center of the point source does not accurately coincide with a pixel center on the sensor. Subpixel shifts with respect to each peak's center and the targeted pixel's center may need to be considered in order to get a well-centered PSF.

These measurement show noise in the range of 10^{-5} with respect to the peak intensity.

2.4.2. Averaging process

When plotted on a logarithmic intensity scale, the PSF measurements differ visibly over the different sensor locations and wavelengths. Nevertheless, in this work, we consider deconvolution approaches assuming the signal to be degraded by a single, spatial and spectral non-varying PSF. In order to derive a single PSF from all 30 PSF instances, we considered different aggregation approaches as discussed in the following paragraphs.

Pixel-accurate shifting of an equidistantly sampled signal is simple to perform, as the signal stays on the pixel grid. For strongly peaked signals, one can simply take the position of maximum and shift the signal such that the peak coincides with a predefined pixel location, e.g. the center of the image. Pixel-accurate shifting has the advantage, that no interpolation of the shifted signal is needed. This is especially important, when dealing with highly peaked signals like the PSF measurements, where interpolation can introduce severe artifacts. Subpixel-accurate shifting can easily be implemented in Fourier domain, where interpolation is done implicitly (by sinc-interpolation). However, peaked signals often produce severe ringing artifacts, which can be reduced e.g. by suitably increasing resolution before shifting and reducing it afterwards. Nevertheless, hard to control artifacts remain, making results unreliable.

A clear disadvantage of pixel-accurate shifting is that subpixel shifts present in the measurements are not corrected and thus produce an up to 1 pixel diameter jitter between the aligned PSF measurements. When simply averaging over the aligned PSF measurements, this jitter introduces additional blur to the resulting PSF. However, closely inspecting the measured PSFs, we observe, that the dominant part of them are not only monotonically decreasing with increasing distance from the peak, but they are mostly convex, i.e. their second order derivative is positive almost everywhere except at the very peak location. For such PSFs, we may use other aggregation methods than averaging to reduce blurring or even sharpen the outcome. To explain this effect, consider a pixel left of the peak of a PSF. Comparing the effect of displacements away from the ideal centered position, from the monotonic behavior it follows, that when moving the PSF to the right, the value observed at this pixel location will decrease. When moving the PSF to the left, the value observed at this pixel location will increase. As the signal is convex here, values increase stronger for off-center displacements to the left than they decrease for the same displacement to the right. Consequently, when observing a representative set of randomly sampled instances of such a PSF at the same pixel location left off center, their mean will increase, resulting in a larger width of the PSF. Using the

median instead of the mean suppresses this effect. When we assume, that the positioning of the point source for calibration has been done independently of the pixel grid, we expect the distribution of the true peak positions be uniformly distributed over the center pixel's area. Then, the median position of the center is close to the middle of the center pixel. Thus the median delivers a PSF being as wide as the measured PSFs. At the peak location, the maximum is selected, corresponding to the best centered PSF.

We call the PSF derived by mean φ_{mean} and by median φ_{median}.

2.4.3. Sharpening PSFs

Both PSFs φ_{mean} and φ_{median} are derived from calibration data being blurred by the light source's, i.e. the monochromator's PSF φ_{source} (see Section 2.4.1). Thus, in order to make φ_{mean} and φ_{median} as similar to the unknown real PSF of the FLUO module, they should be deconvolved with φ_{source}. To this end, without having more information on φ_{source} than its spectral component being 0.14 nm wide, we model φ_{source} as Gaussian. The spectral width of 0.14 nm corresponds to $\sigma_s = 0.07$ nm $=$ 1.27 pix. For the spatial width, we observe in Fig. 3, that the measured PSF, being the unknown true PSF φ_{true} of the FLUO sensor convolved with the PSF φ_{source} of the light source, is sharper in spatial direction than spectral direction. Assuming that half of the overall spatial width can be accounted to the light source and the other half to the FLUO sensor, leads to a spatial component $\sigma_x = 0.8\,pix$ for φ_{source}. We use the same σ_x for the simulated, synthetic PSF $\varphi_{\text{true,synth.}}$ of the sensor (see also Section 2.5). Larger σ's for φ_{source} lead to sharper PSFs for the FLUO sensor after deconvolution and thus to less sharpening and less noise amplification of the measured spatio-spectral data later on. Please note, that the uncertainty on the spatial part of the PSF of the light source used for calibration has no negative effect on the validity of our study, as quantitative experiments are performed on fully synthetic data, where this parameter is known.

We deconvolve both PSFs φ_{mean} and φ_{median} using seven iterations of Lucy-Richardson deconvolution with φ_{source} and get $\varphi_{\text{mean,Lucy}}$ and $\varphi_{\text{median,Lucy}}$. In pre-experiments on convolution and deconvolution of peaked PSFs with Gaussians seven iterations provided pertinent sharpening in a fully simulated setting. Fig. 3 depicts the four different PSFs used in our experiments with real data.

2.5. Synthetic data and simulated calibration

In order to be able to quantify effects of PSF aggregation (Section 2.4.2) and PSF sharpening (Section 2.4.3) on hyperspectral image deconvolution, we simulated the full calibration process as well as imaging. To this end, we defined a ground truth PSF $\varphi_{\text{true,synth.}}$ being a Gaussian with a spatial standard deviation $\sigma_x = 0.8\,pix$ and spectral $\sigma_s =$ 0.11 nm $=$ 2 pix. We selected σ_x and σ_s such that convolving $\varphi_{\text{true,synth.}}$ with the PSF of the monochromator φ_{source} yields a PSF being in the peak region very similar to the measured φ_{mean} (cmp. the corresponding PSFs in Figs. 3 and 4).

2.5.1. Synthetic calibration data

We synthetically generated PSF calibration data by generating $\varphi_{\text{true, synth.}}$ convolved by φ_{source} at the same 30 spatial-spectral positions, where the real calibration data has been measured (cmp. Section 2.4.1). The data is scaled to the same maximum value as the real calibration data and the same 'dark' background value. Finally Poisson noise as in the real calibration data has been added.

2.5.2. Synthetic point spread functions

Synthetic PSFs $\varphi_{\text{mean,synth.}}$, $\varphi_{\text{mean,Lucy,synth.}}$, $\varphi_{\text{median,synth.}}$, and $\varphi_{\text{median, Lucy,synth.}}$ (see Fig. 4) are derived following Sections 2.4.2 and 2.4.3, i.e. running the same script, but using the synthetic calibration data from Section 2.5.1 instead of real calibration data.

In the experiments below (Section 3.1), we compare the performance of all four synthetic PSFs. In addition, we test a well-known way of sharpening a PSF by squaring it ($\varphi^2_{\text{mean,synth.}}$) as proposed by Deneve et al. (1999).

2.5.3. Synthetic spatio-spectral images of plants and soil

The deconvolution task addressed here significantly differs from common tasks like e.g. camera shake removal (Levin et al., 2009). Images are taken under heavily controlled conditions where the blurring is due to a very sharp PSF stemming from a high-end scientific optical system. Further the FLUO module is designed to take spectral images of plants near the O_2 absorption bands. Inspecting typical vegetation spectra (cmp. Figs. 2 and 5), we notice major differences to usual image data used to evaluate computer vision algorithms like photographs of objects (e.g. the ImageNet dataset, Deng et al. (2009)) or city scenes (Cityscapes dataset, Cordts et al. (2016)):

- The mean spectral response of plants, i.e. at sensor radiance, in the range between 670 nm and 780 nm observable by the FLUO module typically starts at values below 2 W/(m^2 sr μm) at 687 nm and increases to over 100 or even 150 W/(m^2 sr μm) at 780 nm, i.e. the signal mean roughly increases about one and a half orders of magnitude.
- Vegetation fluorescence is in the range of 1 to 2 W/(m^2 sr μm) at around 760 nm with a width at half height of approx. 50 nm.
- The signal part interesting for fluorescence retrieval is therefore in the absorption bands producing sharp valleys in the signal. These parts of the signal need to be reconstructed with high accuracy to allow for as accurate as possible SIF retrieval, as we will investigate in our experiments below (see Section 3.3.

Well established test images from computer vision are therefore not suitable here. In order to get as close as possible to our application scenario, we synthetically compose spatial spectral images $I_{\text{true}}(\lambda, x, t)$ which we can use as ground truth data. To this end we take the real 1024×384×301 data I_{real} described in Section 2.2, and exchange the real measured spectra by simulated ones. To be more precise, at each 2d spatial position (x, t) in $I_{\text{real}}(\lambda, x, t)$, we calculate the mean intensity over

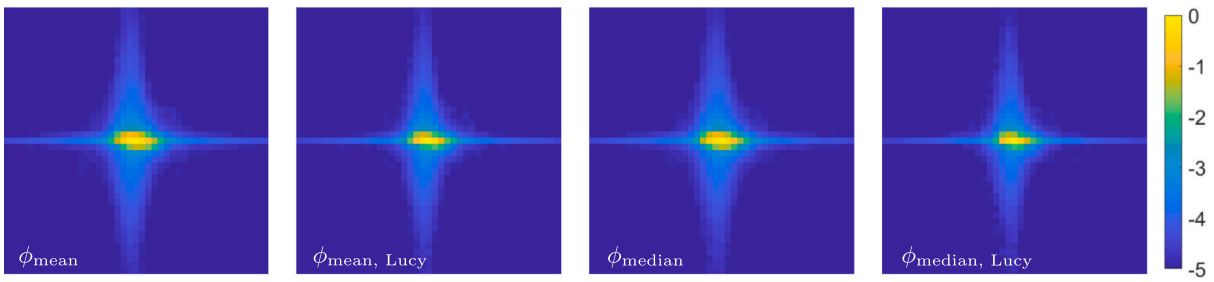

Fig. 3. PSFs from real calibration data: Mean and median aggregated PSFs and their sharpened versions φ_{mean}, $\varphi_{\text{mean,Lucy}}$, φ_{median}, and $\varphi_{\text{median,Lucy}}$. The center 43×43 pixels are shown, where the horizontal axis is spectral and the vertical axis spatial. Please note the logarithmic scaling (base 10) of the color-coded unit free PSF values, normalized to sum up to 1.

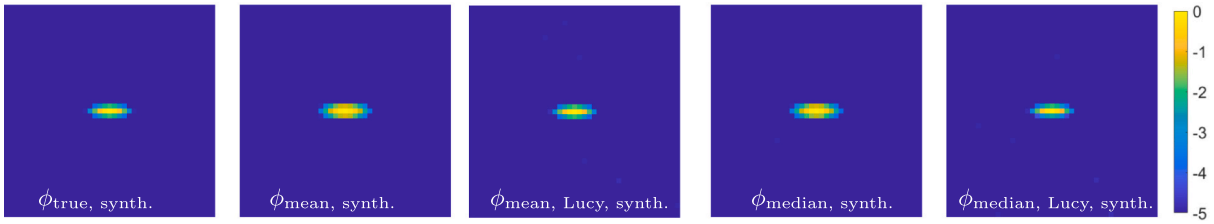

Fig. 4. PSFs from synthetic calibration data: Ground truth, mean and median aggregated PSFs and their sharpened versions $\varphi_{\text{true,synth.}}$, $\varphi_{\text{mean,synth.}}$, $\varphi_{\text{mean,Lucy,synth.}}$, $\varphi_{\text{median,synth.}}$, and $\varphi_{\text{median,Lucy,synth.}}$. The center 43×43 pixels are shown, where the horizontal axis is spectral and the vertical axis spatial. Please note the logarithmic scaling (base 10) of the color-coded unit free PSF values, normalized to sum up to 1.

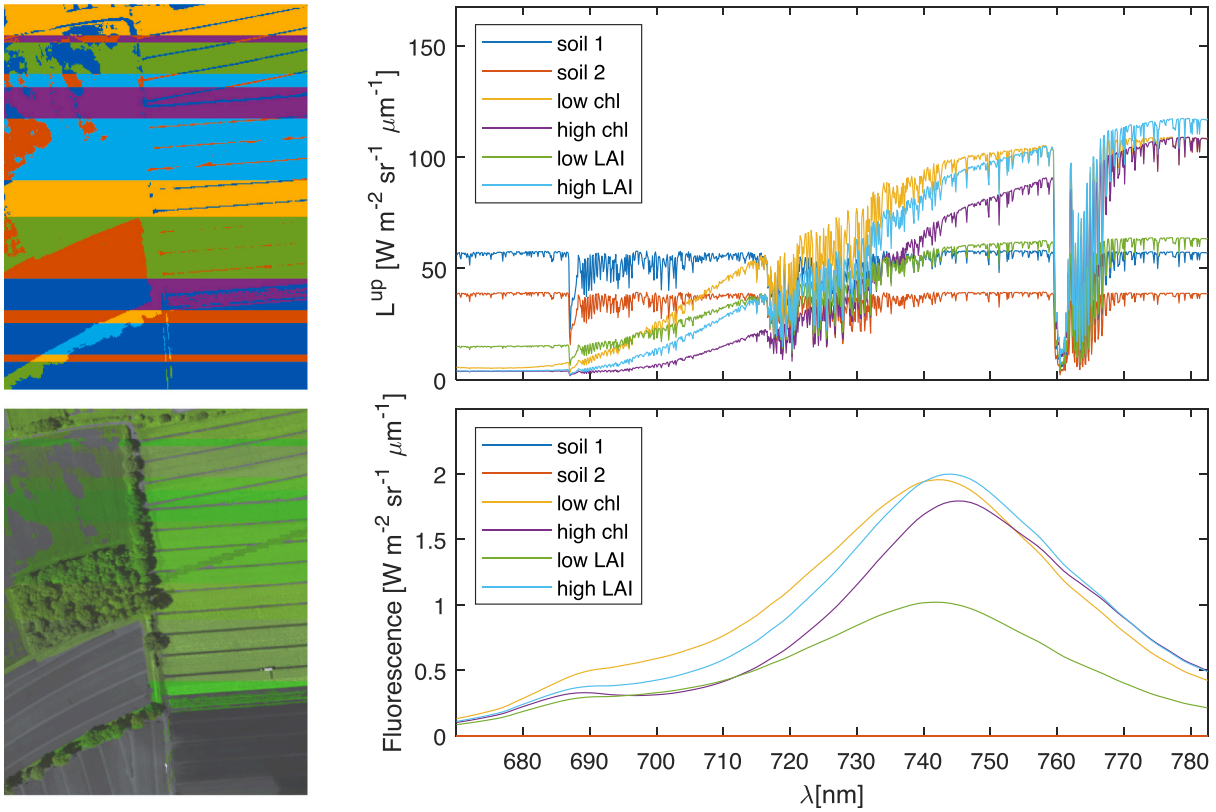

Fig. 5. Spatial-spectral synthetic images. Top: Six synthetic spectra $I_s(\lambda)$ (right) and index image $s(x, t)$, i.e. where they are to find in the synthetic data (left, line colors and colors of the index image coincide). Bottom left: Synthetic spatio-spectral data I_{true} mimicking I_{real} by construction. It is shown in the same pseudo colors as I_{real} in Fig. 2, left. Bottom right: synthetic fluorescence signal contained in the simulated spectra $I_s(\lambda)$.

the whole spectrum $\bar{I}_{\text{real}}(x,t) = \sum_\lambda I_{\text{real}}(\lambda,x,t)/1024$. The spectral components $I_s(\lambda)$, $s \in \{1,\ldots,6\}$, of six different targets are from physical spectra simulations. Radiative transfer through plant canopy has been simulated using SCOPE (version v1.73, (Tol et al., 2009)) and atmosphere radiative transfer was simulated using MODTRAN5 (Berk et al., 2004). SCOPE and MODTRAN are well-established tools designed for spectrally resolved radiative transfer simulation. Please find their parameterization used in this study in the supplemental material (Section Appendix A.1). Radiance spectra bottom of atmosphere of four different vegetation parameterizations, i.e. vegetation with low or high chlorophyll content and low or high Leaf Area Index (LAI), and two soil types were simulated containing specific fluorescence signals (Fig. 5, right, top and bottom). The spectra have mean intensities $\bar{I}_s$. To distribute $I_s(\lambda)$ for vegetation and soil as in the real data, we find vegetation at positions (x, t) according to the 'Ratio Vegetation Index' (NIR/Red) (see e.g. Jordan, 1969), i.e. where $I_{\text{real}}(757.8\,nm, x, t)/I_{\text{real}}(678.68\,nm, x, t) > 1.45$. In the synthetic data, we use simulated soil spectra for non-vegetation, and vegetation spectra for vegetation. We define a distribution pattern, where at each x the vegetation or soil is constant for the whole flight time, i.e. for all t. This yields a striped index pattern $s(x, t)$, cmp. Fig. 5, top left. The synthetic data $I_{\text{true}}(\lambda, x, t)$ is then given by $I_{\text{true}}(\lambda,x,t) = \bar{I}_{\text{real}}(x,t) I_{s(x,t)}(\lambda)/\bar{I}_{s(x,t)}$.

As input data for our synthetic deconvolution experiments we need suitably corrupted data $I_{\text{corr}}(\lambda, x, t)$. We derive it by convolving I_{true} by the ground truth PSF $\varphi_{\text{true,synth.}}$ and adding shot noise from the noise distribution known from radiometric calibration (cmp. Section 2.3).

2.6. Retrieval of sun induced fluorescence

As our finally desired signal is the sun induced fluorescence (SIF) from O_2A and O_2B bands, we apply a specialized SIF retrieval method, i.e. the improved Fraunhofer Line Discrimination Method (iFLD, originally developed by Alonso et al. (2008) and refined by Damm et al. (2014)). The main idea behind this algorithm is that at wavelength λ radiance $L(\lambda)$ coming from a target with reflectance $R(\lambda)$ depends on the incoming irradiance $I(\lambda)$ and fluorescence $f(\lambda)$ via $L(\lambda) = R(\lambda)I(\lambda) + f(\lambda)$.

The standard FLD method assumes that for two wavelengths λ_1 and λ_2 being close enough reflectance R and fluorescence f can be assumed to be constant, $R := R(\lambda_1) = R(\lambda_2)$ and $f := f(\lambda_1) = f(\lambda_2)$ for $\lambda_1 \approx \lambda_2$. Thus when irradiances $I(\lambda_1)$ and $I(\lambda_2)$, and radiances $L(\lambda_1)$ and $L(\lambda_2)$ are known, one can solve for f and R. Measurement noise has least influence on the estimation of f, when λ_1 and λ_2 lie inside and outside of an absorption band, respectively.

The iFLD method relaxes the FLD's constancy assumptions for R and f by setting $R(\lambda_1) = \alpha_R R(\lambda_2)$ and $f(\lambda_1) = \alpha_F f(\lambda_2)$. For plants the two parameters α_R and α_F can e.g. be derived from functional simulations on reflectance and fluorescence mechanisms i.e. we use the expected value of $R(\lambda_1)/R(\lambda_2)$ and $f(\lambda_1)/f(\lambda_2)$ in the O_2A and O_2B bands.

2.7. Error measures

We evaluate errors using bias, Root Mean Squared Error (RMSE), and the Peak Signal to Noise Ratio (PSNR). Bias is the non-squared mean error. For comparing two discrete image signals, I_0 being the ground truth and I_1 the estimated signal, with N sampling points or pixels it reads

$$\text{bias} = \frac{1}{N}\sum_{i=1}^{N}(I_1 - I_0) \tag{9}$$

Negative bias means the signal is on average underestimated, positive overestimated. It should not be confused with RMSE, i.e.

$$\text{RMSE} = \frac{1}{N}\left(\sum_{i=1}^{N}(I_1 - I_0)^2\right)^{\frac{1}{2}} \tag{10}$$

being always non-negative. PSNR is proportional to the logarithm of the inverse RMSE, i.e.

$$\text{PSNR} = 20log\left(\frac{I_{\max}}{\text{RMSE}}\right) \tag{11}$$

where $I_{\max}$ is the maximum radiance value observed in our data, see e.g. Thu and Ghanbari (2008)).

3. Experiments

We first perform experiments on synthetic data in order to quantitatively investigate the different PSF and deconvolution method combinations. We observe different effects which can be explained consistently from theory. Then we apply the same combinations to real spatio-spectral data to see, whether or not the same effects appear.

3.1. Deconvolution of synthetic spatio-spectral data

On this data, in a training step, we derived optimal iteration numbers for the vanCittert, Lucy-Richardson, and blind deconvolution algorithms. We evaluate errors using PSNR, see Section 2.7, Eq. (11). We found that 3 iterations yield highest PSNR values for vanCittert's method, independent of which PSF is used. For Lucy-Richardson and blind deconvolution about 7 iterations are best for the non-sharpened PSFs $\varphi_{\text{mean,synth.}}$ and $\varphi_{\text{median,synth.}}$, and 12 iterations for the sharper ones $\varphi_{\text{true,synth.}}$, $\varphi_{\text{mean,Lucy,synth.}}$ and $\varphi_{\text{median,Lucy,synth.}}$. As blind deconvolution yielded always very similar results as Lucy-Richardson (PSNR difference about 0.1%), we omit results on blind deconvolution in the following. The tested blind deconvolution is Lucy-Richardson deconvolution with an additional update step on the PSF (see Section 2.1, Eq. (5)). We conclude that this step has no relevant effect when operating on our already very peaked PSFs.

3.1.1. Quantitative results in terms of PSNR

We computed deconvolution results using the six different remaining algorithms, namely 1 or 3 iterations of vanCittert's algorithm, regularized deconvolution, Wiener filtering, and 7 or 12 iterations of Lucy-Richardson algorithm. We ran each algorithm with each of the six different PSFs derived above, namely $\varphi_{\text{true,synth.}}$, $\varphi_{\text{mean,synth.}}$, $\varphi_{\text{mean,Lucy,synth.}}$, $\varphi_{\text{median,synth.}}$, $\varphi_{\text{median,Lucy,synth.}}$, and $\varphi^2_{\text{mean,synth.}}$. Results are depicted in Fig. 6, where we show PSNRs for all of these combinations as bar plots. Fig. 6**A** shows PSNRs for the full signal, **B** and **C** for the O_2A band and O_2B band, respectively.

For the baseline, 1 iteration of vanCittert's algorithm (see Siegmann et al. (2019)), we observe in Fig. 6**A**, that the exact shape of the PSF has only minor influence on the result, when being interested in the full spectrum where values vary between PSNR 36.4 and 36.7 with standard deviations of 1.7 . Please refer to Table A.3 for mean and standard deviations of PSNR values. In Fig. 6**B** the same behavior can be seen for the O_2A band where PSNR also varies non-significantly between 29.9 and 30.8 with standard deviation of 2.2. For the O_2B band in Fig. 6**C** using sharpened PSFs is crucial, as the unsharpened ones $\varphi_{\text{mean,synth.}}$ and $\varphi_{\text{median,synth.}}$ even slightly deteriorate the signal.

In Fig. 6**A**, for all the other algorithms we observe, that, non-surprisingly, using the true PSF $\varphi_{\text{true,synth.}}$ works best. PSNR values are 34.9 for the unchanged signal, 36.7 when applying vanCittert1, 38.3 for vanCittert3, 38.8 for deconvreg, 40.27 for deconvwnr, and 38.0 and 38.6 for LucyRichards7 and LucyRichards12, respectively. The deconvolved PSFs $\varphi_{\text{mean,synth.,Lucy}}$ and $\varphi_{\text{median,synth.,Lucy}}$ yield no significant differences to the true PSF, and $\varphi^2_{\text{mean,synth.}}$ is only a little worse, such that in the barplot differences are hard see and clearly much smaller than the standard deviations. Using the non-sharpened PSFs $\varphi_{\text{mean,synth.}}$ and $\varphi_{\text{median,synth.}}$ systematically does not reach the improvements achieved by the other PSFs. This behavior is stronger, for algorithms with less regularization in high-frequent signal parts.

Three iterations of vanCittert's algorithm yield stable improvements almost independent of the PSF used. Deconvreg and the two versions of Lucy-Richardson show simular behavior, where deconvolved PSFs slightly outperform the others including $\varphi^2_{\text{mean,synth.}}$. Wiener filtering should only be used with suitably sharpened PSFs where PSNR is up to 40.2, as performance drops strongly when using too smooth PSFs $\varphi_{\text{mean,synth.}}$ (PSNR 34.5) and $\varphi_{\text{median,synth.}}$ (PSNR 36.0), and only slightly improves using the squared $\varphi^2_{\text{mean,synth.}}$ (PSNR 39.0). However, when using suitable PSFs, Wiener filtering yields highest signal improvements of all tested algorithms.

For the O_2A band in Fig. 6**B** we observe a similar behavior as for the full spectrum in Fig. 6**A**. For regions with low signal strength as the O_2B band, results shown in Fig. 6**C**, using a suitable PSF is crucial. If doing so, all algorithms yield signal improvements, and using Deconvreg or Wiener filtering yield similar best performance.

Overall, comparing the algorithms in cases where the signal is improved, Wiener filtering outperforms the other approaches in terms of PSNR, but also deteriorates the signal most, when PSFs are too smooth. For the O_2B band, the only way to achieve an improvement using the proposed methods is using a suitably sharp PSF as using $\varphi_{\text{mean,synth.}}$ and $\varphi_{\text{median,synth.}}$ always deteriorates the signal. When only interested in the O_2A band, applying 3 iterations of vanCittert's algorithm robustly yields good deconvolution perfomance, also with too smooth PSFs like $\varphi_{\text{mean,synth.}}$ and $\varphi_{\text{median,synth.}}$. Results are on a par with Lucy-Richardson with 12 iterations and regularized deconvolution for the sharpened PSFs and always better than 1 iteration of vanCittert's algorithm.

Comparing overall performance of the different PSFs, we observe that if significant differences are present for an algorithm, sharpened PSFs $\varphi_{\text{mean,Lucy,synth.}}$, $\varphi_{\text{median,Lucy,synth.}}$, and $\varphi^2_{\text{mean,synth.}}$ perform better than non-sharpened $\varphi_{\text{mean,synth.}}$ and $\varphi_{\text{median,synth.}}$. The performance of squared $\varphi^2_{\text{mean,synth.}}$ in the full spectrum or O_2A band either belongs to the worst group (vanCittert and deconvreg algorithms), or lies between deconvolved and unsharpened PSFs (Wiener filter and Lucy-Richardson algorithms). In the O_2B band its performance shows no significant

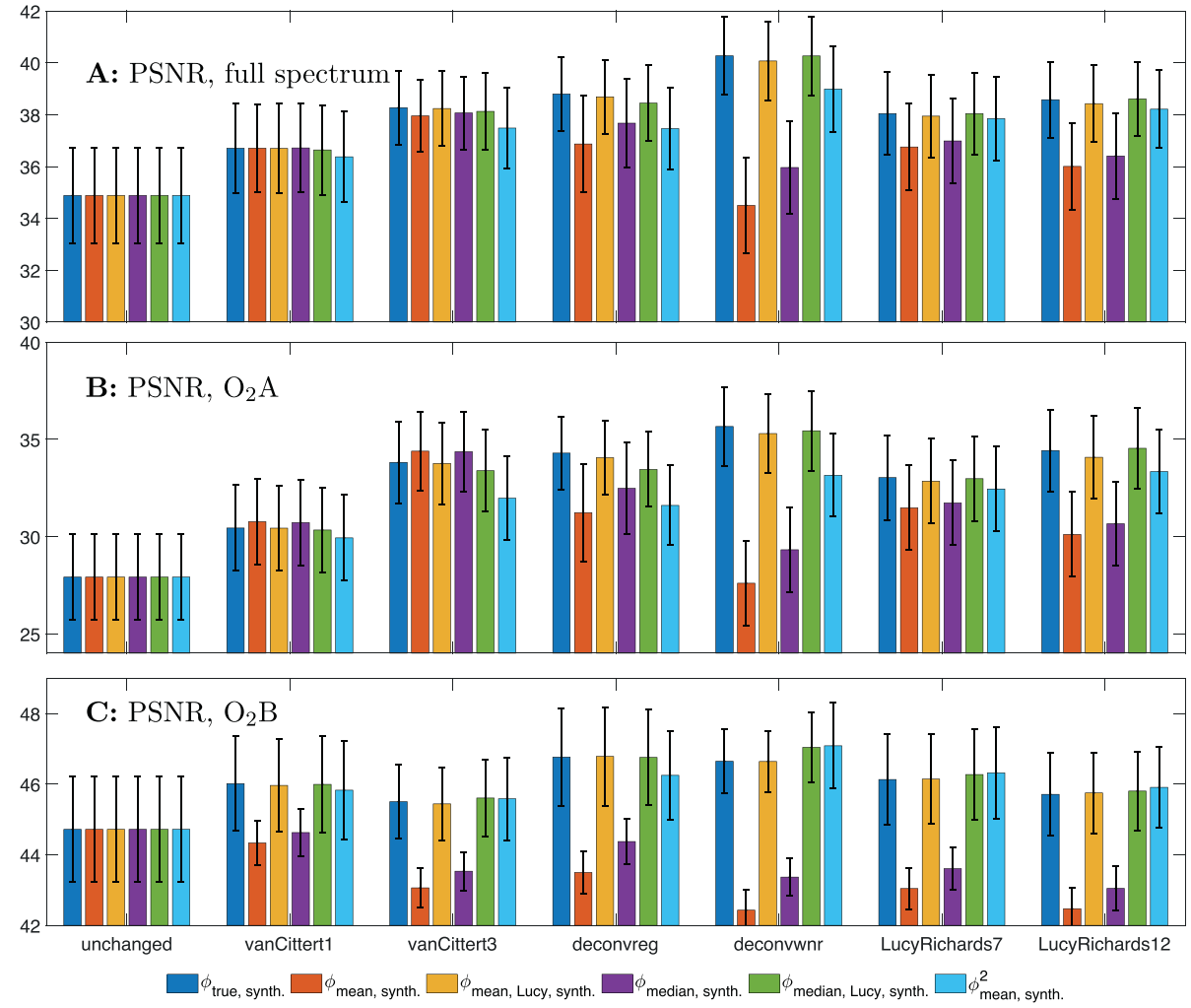

Fig. 6. Mean PSNR values (unit free) and their standard deviations for different deconvolution algorithms and using different PSFs. Larger values indicate better signal quality. 'Unchanged' describes PSNR of the initial data. Please compare Table A.3.

difference to deconvolved or the true PSF. Overall it does not stick out positively or negatively. The deconvolved PSFs $\varphi_{\text{mean,Lucy,synth.}}$ and $\varphi_{\text{median,Lucy,synth.}}$ consistently yield no significant difference to using the ground truth PSF $\varphi_{\text{true,synth.}}$.

3.1.2. Qualitative results

In order to get an impression of the deconvolution effect, we show in Fig. 7**A–D** a row, i.e. spectrum, from our synthetic data before corrupting, i.e. the ground truth, after applying the PSF and noise, and the reconstructions derived using vanCittert, Lucy-Richardson, and Wiener filtering.

We omit deconvolution results from regularized deconvolution for better overview. We observe, that for $\varphi_{\text{mean,synth}}$ and $\varphi_{\text{median,synth}}$ the reconstructed spectra do not match well with the initial data, as the overall amplitude is too high in high signal regions and too low in low signal parts. This effect comes from too wide spatial reach of these PSFs. The other two, sharpened PSFs $\varphi_{\text{mean,Lucy,synth.}}$ and $\varphi_{\text{median,Lucy,synth.}}$ yield very similar, plausible results that need further inspection for a detailed analysis. We therefore zoom in at the O_2A band for the result using $\varphi_{\text{median,Lucy,synth.}}$ and contrast them to the results using $\varphi_{\text{mean,synth}}$ in Fig. 7**E–J**. In Fig. 7**H** and **J** we see that the different algorithms correct the corrupted signal differently strong. VanCittert with 1 iteration makes the least change, VanCittert with 3 iterations changes more and Lucy-Richardson and Wiener filtering even more. Using the too smooth $\varphi_{\text{median,synth}}$ this leads to overcorrection for Lucy-Richardson and Wiener Filtering. VanCitter with 3 iterations comes close to the original signal. Using the sharper $\varphi_{\text{median,Lucy,synth.}}$ Lucy-Richardson and Wiener Filtering come even closer to the desired original signal.

For the less pronounced O_2B band shown in Fig. 7**K,L** differences are more clearly visible. Using $\varphi_{\text{mean,synth}}$ offsets the signal towards lower values due to the too smooth spatial component. In addition, especially well visible for Wiener filtering, high-frequent oscillations are amplified more than desired. Using $\varphi_{\text{median,Lucy,synth.}}$ the overall offset is no longer visible and oscillations are less pronounced.

We conclude, that the qualitative inspection is consistent with the quantitative observations: Lucy-Richardson and Wiener filtering perform well when a suitably sharp PSF is available, but overcorrect, when not. If unsure, it may be better to use vanCittert's algorithm with 3 iterations, performing reliably well, even if not reaching the performance of the other two algorithms in good cases.

3.2. Deconvolution experiments on real data

For real data no ground truth is available. However, for the spectral components some physics-based features can be observed in order to judge reconstruction quality:

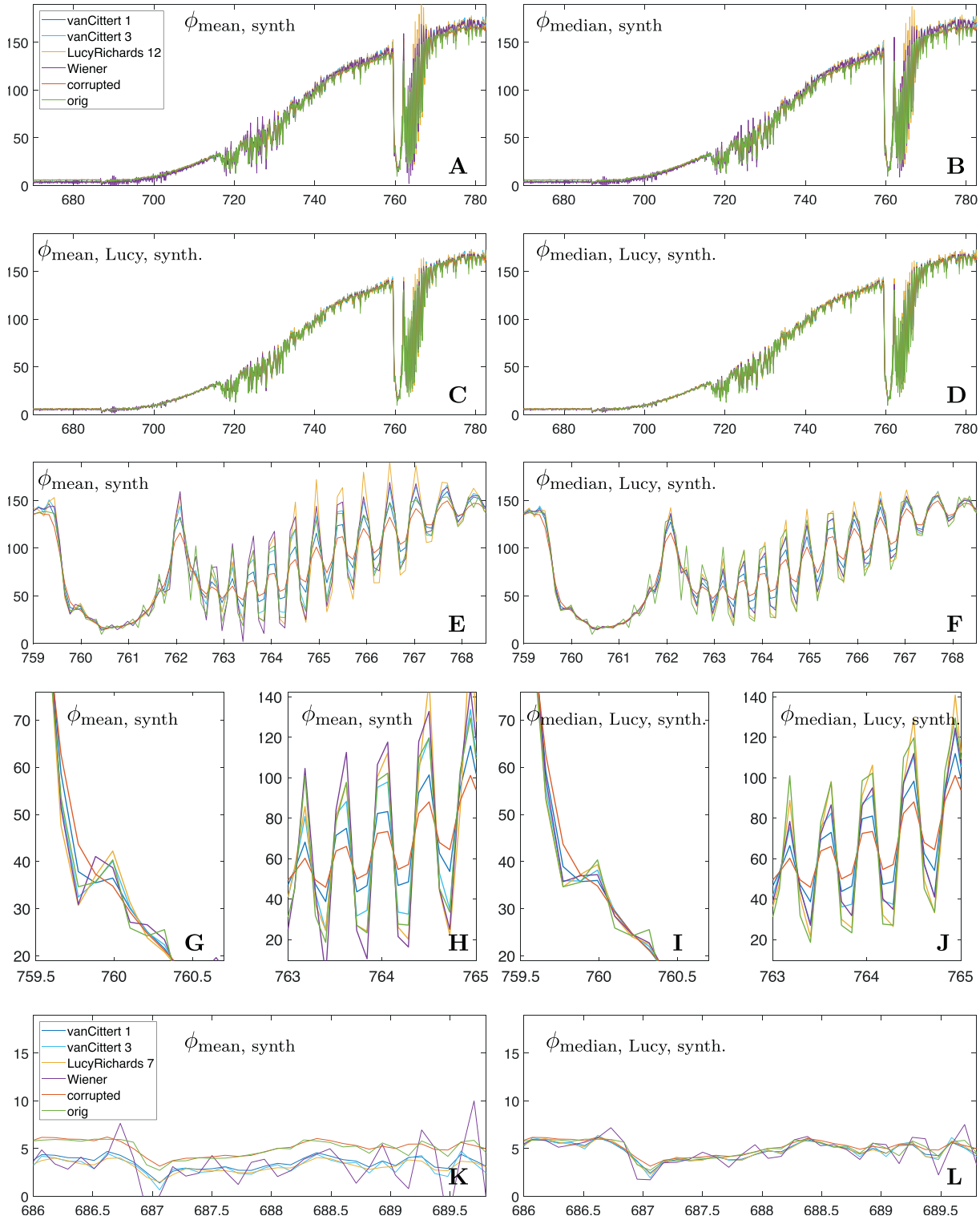

Fig. 7. Deconvolution results for one spectral line from our synthetic dataset, spectral response in W/(m^2 sr μm) versus wavelength in nm. **A–D:** Full spectra for four different PSFs. **E–J:** O_2A band and details of it, left for $\varphi_{\text{mean,synth}}$, right for $\varphi_{\text{median,Lucy,synth.}}$. **K,L:** O_2B band, left for $\varphi_{\text{mean,synth}}$, right for $\varphi_{\text{median,Lucy,synth.}}$. Legend in **A** is valid for plots **A–J**. Legend in **K** is valid for plots **K** and **L**.

- Ringing: For absorption bands it is clear, that they are steep drops in an otherwise mainly smooth spectrum. Thus the upper borders of bands in a reconstructed spectrum should not show strong overshoots. Such overshoots stem from over-amplification of signal or noise, indicating either that the noise level has been estimated too low, or the PSF used for deconvolution is smoother than the true PSF and thus the signal is over-corrected. However, as our data contains some noise, for an optimal reconstruction we expect ringing artifacts in the same range as the noise amplitude. For example, see the overshoots of LucyRichards 12 in Fig. 7**A,B** in the O_2A band from 765 nm to 767 nm or of Wiener filtering and LucyRichards 12 in Fig. 8**A–C**.

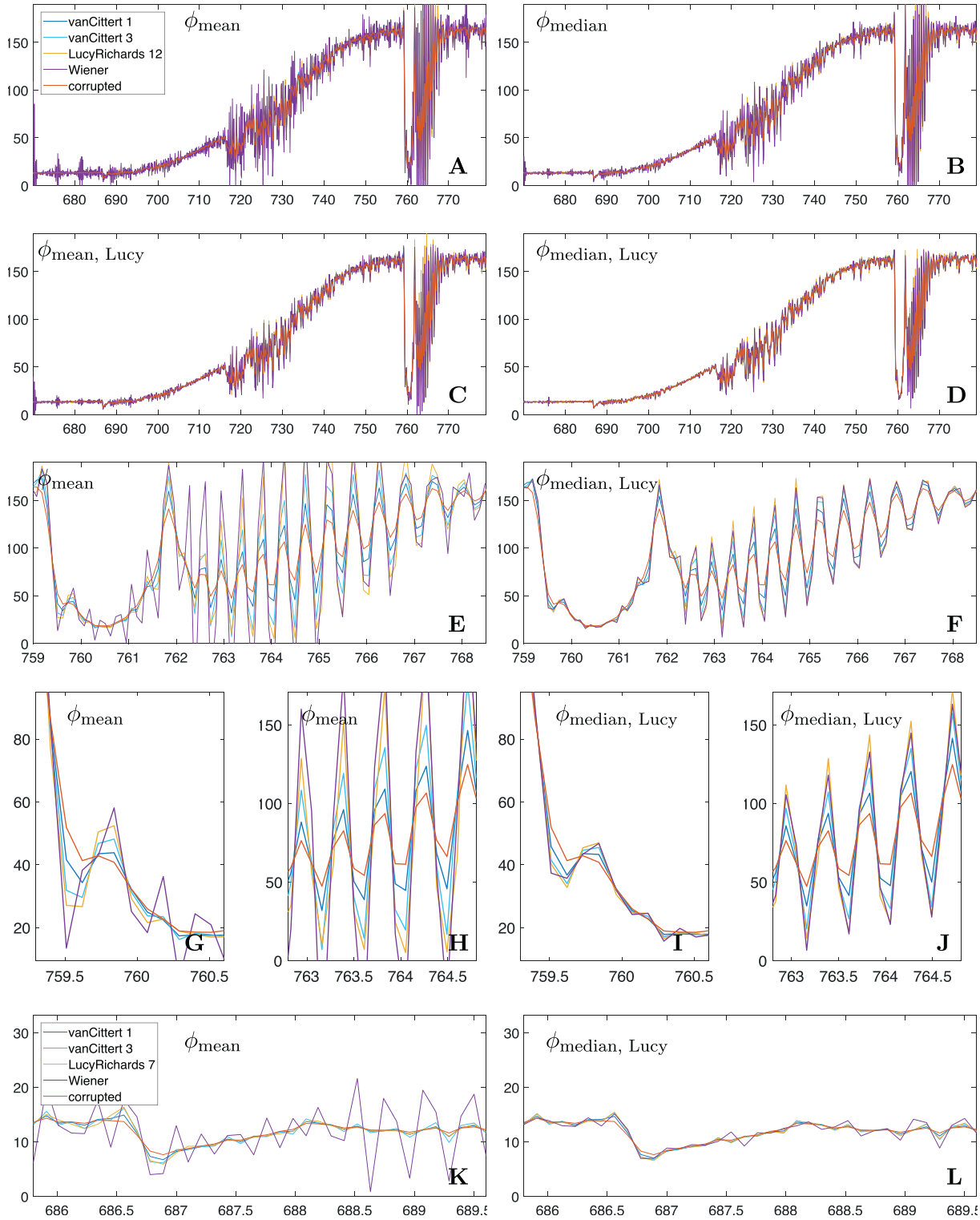

Fig. 8. Deconvolution results for one spectral line from our real dataset, spectral response in W/(m^2 sr μm) versus wavelength in nm. **A–D:** Full spectra for four different PSFs. **E–J:** O_2A band and details of it, left for φ_{mean}, right for $\varphi_{\text{median,Lucy}}$. **K,L:** O_2B band, left for φ_{mean}, right for $\varphi_{\text{median,Lucy}}$. Legend in **A** is valid for plots **A, J**. Legend in **K** is valid for plots **K** and **L**.

- Positivity: Spectra need to be positive everywhere, especially in the deepest valleys of absorption bands, as the noise level in our data is small. For example, see the undershoots of Wiener filtering in Fig. 8**A,B** and **E** in the O_2A band from 762.5 nm to 765 nm.
- Under-correction: Too little correction by a deconvolution scheme can be detected, by re-applying the PSF to the deconvolved image. Convolving a good deconvolution result with the PSF should yield a signal close to the initial raw data. Here 'close' means in the same range as the noise level. If the re-convolved data is significantly smoother than the raw data, then the deconvolution scheme did not sharpen the signal enough. In such cases, sharp peaks and valleys are visibly reduced.

Thus the absence of strong ringing artifacts as well as positive signal values indicate good reconstruction quality. Absence of ringing indicates possible under-correction of PSF blurring.

When we deconvolve our real test data using the Wiener filter together with the PSF φ_{mean} stemming from averaging PSF calibration measurements, we observe wild over and undershoots in the O_2A band region (see Fig. 8**A**). This indicates, that this PSF is smoother than the actual PSF as concluded above. Same is true when using φ_{median} and less severely for $\varphi_{\text{mean,Lucy}}$. When we deconvolve with the sharpest PSF in this test, i.e. $\varphi_{\text{median,Lucy}}$, we observe that over- and undershoots are much smaller (see Fig. 8**D**). For a more detailed analysis, we again show zoom-ins on the O_2A and O_2B bands (Fig. 8**E–L**). For deconvolutions using φ_{mean} we see in Fig. 8**E** and **H** that strong over and undershoots are mainly present for Lucy-Richardson and Wiener filtering. Reconvolving this data with φ_{mean} (cmp. Fig. 9**B**) reveals that the vanCittert's and also Lucy-Richardson's algorithms undercorrect, even though Lucy-Richardson's algorithm leads to strong oscillations. This is a clear sign, that φ_{mean} is smoother than it should be. Spectra are plausibly reconstructed for $\varphi_{\text{median,Lucy}}$, in Fig. 8**F, I** and **J** with a similar behavior as in the synthetic data shown in Fig. 7. Lucy-Richardson and Wiener filtering show similar reconstructions as vanCittert 3 with φ_{mean}. In the O_2B band, apart from the obvious too high oscillations for Wiener filtering using φ_{mean}, no clear differences are visible for the different methods.

Overall we see a similar behavior as for the synthetic data, thus using sharpened PSFs and either vanCitters algorithm with 3 iterations or Lucy-Richardson or Wiener filtering seems to be beneficial. In order to test the different solutions capabilities for our target application, we investigate their performance when the deconvolved signal is used for fluorescence retrieval.

3.3. Experiments with fluorescence retrieval from synthetic data

In order to get insight in the effect of PSF deconvolution for our target application, i.e. retrieval of sun-induced fluorescence (SIF), we applied the iFLD algorithm described in Section 2.6 to the deconvolved synthetic data from the experiment shown in Section 3.1. O_2A- and O_2B bands were processed independently, where for O_2A SIF at wavelength 760 nm has been evaluated and for O_2B at wavelength 687 nm, denoted SIF_{760} and SIF_{687}, respectively. The known true synthetic SIF data for these wavelengths is shown in Fig. 10B and C. The mean value of SIF_{760} is 0.526 W/(m^2 sr μm) and of SIF_{687} it is 0.168 W/(m^2 sr μm).

In Fig. 10D and F we show the root mean squared error (RMSE) of SIF_{760} and SIF_{687} as barplots, where the error bars indicate the standard deviation of the squared error scaled appropriately to RMSE. Surprisingly, higher PSNR of the spectral signal as shown in Fig. 6 does not always lead to more accurate SIF estimates and the other way round. Especially the clear signal improvements achieved using 1 iteration of vanCitterts algorithm (cmp. Fig. 6A) which are more or less independent from the selected PSF, lead to marginally better SIF_{760} estimates for the sharpened PSFs $\varphi_{\text{mean,Lucy,synth.}}$ and $\varphi_{\text{median,Lucy,synth.}}$, and even somewhat worse SIF_{760} estimates for the non-sharpened PSFs $\varphi_{\text{mean,synth.}}$ and $\varphi_{\text{median,synth.}}$. The same is true for the two tested variants of Lucy-Richardson's algorithm, where the positive effect of sharpening PSFs is stronger. For 3 iterations of vanCittert, regularized deconvolution, and Wiener filtering RMSE of SIF_{760} becomes lower with stronger correction. Unexpectedly, the drop in PSNR observed with Wiener filtering and the too smooth, unsharpened PSFs $\varphi_{\text{mean,synth.}}$ and $\varphi_{\text{median,synth.}}$ (cmp. Fig. 6A and B) does not lead to worse SIF_{760} estimates. When looking at the bias, i.e. the non-squared mean error, of the SIF_{760} estimates in Fig. 10E, we see that while all methods overestimate SIF_{760} systematically, overcorrection with Wiener filtering and too smooth PSFs leads to underestimation of SIF_{760}. This behavior can also be observed in Fig. 11, top, when comparing the true SIF map with the two results of Wiener filtering. We conclude that signal degradation introduced by overcorrection via Wiener filtering does not catastrophically destroy SIF_{760}, but only gently suppresses it. Smallest RMSE in the presented experiments on SIF_{760} retrieval is 0.258 W/(m^2 sr μm) achieved by Wiener filtering with $\varphi_{\text{median,synth.}}$ and thus yields an average relative error of 49%. This is a strong improvement wrt. previous methods applying one iteration of vanCittert's algorithm with $\varphi_{\text{mean,synth.}}$ yielding an RMSE of 0.984 W/(m^2 sr μm), or 187% relative error (see Fig. 11, top, for comparison).

For SIF_{687} we observe a totally different behavior in Fig. 10F. Generally, all methods, including 'unchanged', yield high RMSE mostly well above 200% relative error. In addition, standard deviations are often very high.

Wiener filtering always degrades SIF_{687} estimates compared to unchanged data, even though with decreased variance. This behavior cannot be explained by PSNR results. In Fig. 11 top right and bottom right, we see that Wiener filtering with sharpened PSFs produces increased SIF values at spatial edges, even in the zero SIF region in the lower left corner soil region. While these increased values do not add much to the error in SIF_{760}, they have high influence on SIF_{687}.

All other methods improve SIF_{687} estimation on average, but not always with acceptably low standard deviations, indicating the low reliability of SIF_{687} estimates. What is more, there is no clear picture on which PSF performs reliably. $\varphi_{\text{mean,Lucy,synth.}}$ performs overall best together with deconvreg (RMSE is 0.259 W/(m^2 sr μm), i.e. 154% relative error), but gives very high standard deviation with 12 iterations of Lucy-Richardson and the highest observed error with Wiener filtering. $\varphi_{\text{median,Lucy,synth.}}$ performs similarly well using deconvreg, but yields high variances with other methods, see also Fig. 11, bottom. When using the somewhat smoother PSFs $\varphi_{\text{mean,synth.}}$ or $\varphi_{\text{median,synth.}}$ RMSE can even be worse than with the unchanged signal when using deconvreg. No clear recommendation can be drawn from this experiment, as all deconvolution algorithms are highly sensitive on the exact fit of the

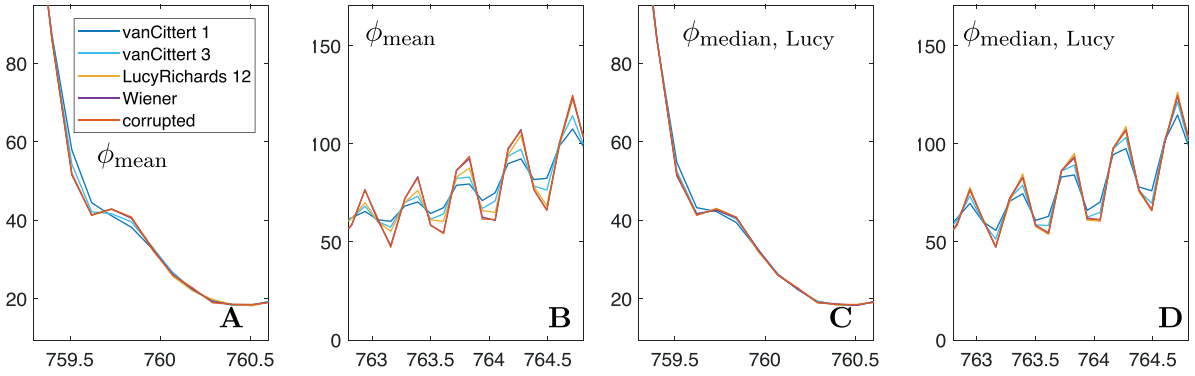

Fig. 9. Results of re-convolution of deconvolved hyperspectral image data for the same line as shown in Fig. 8**G – H**, spectral response in W/(m^2 sr μm) versus wavelength in nm. Legend in Fig. 8**A** is valid here, too.

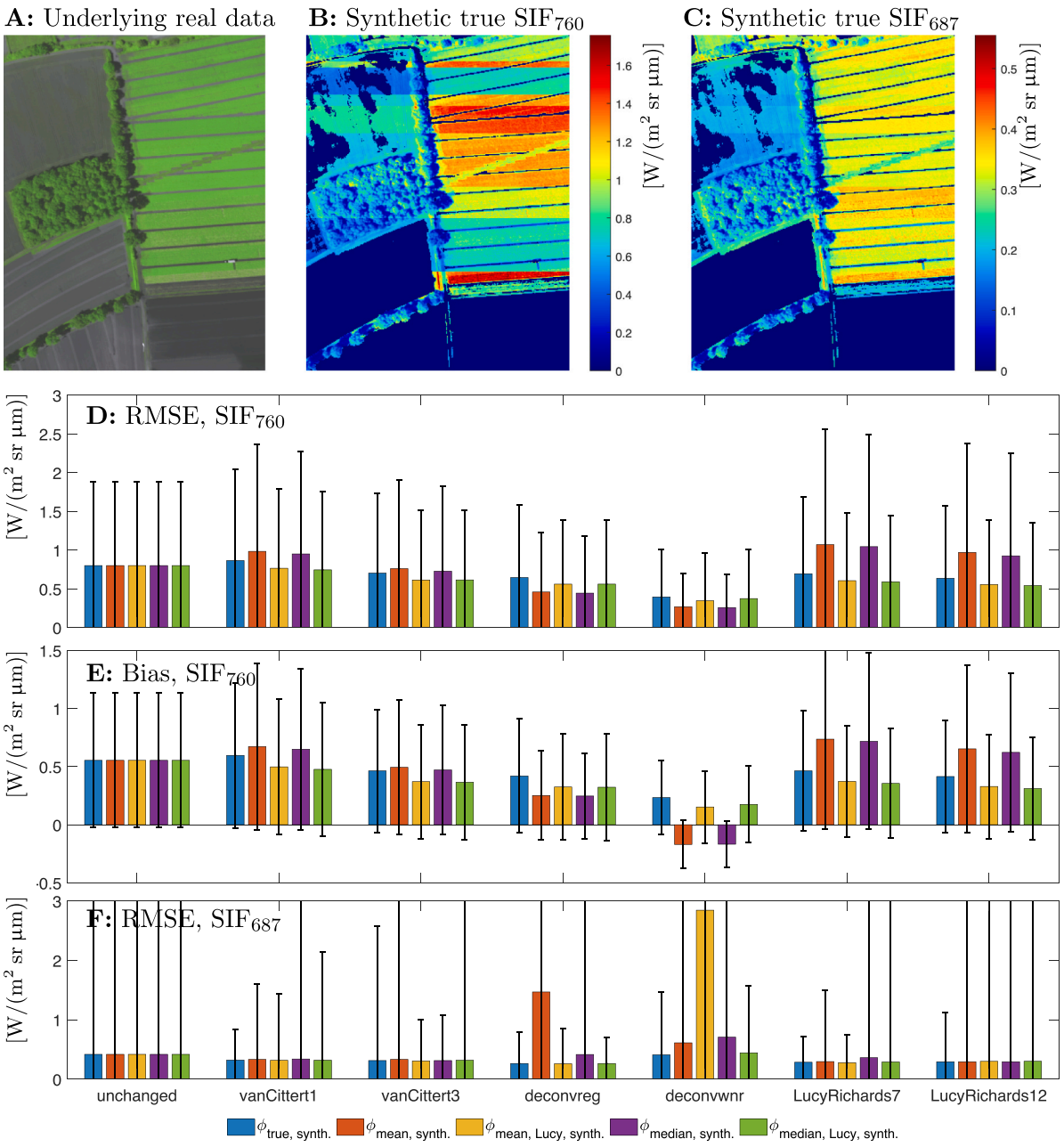

Fig. 10. Estimation of sun-induced fluorescence. A: Spatial component (384×301 pix) of underlying real data I_{real} in pseudo colors, where vegetation is green and soil gray. B and C: True values of SIF_{760} and SIF_{687} in synthetic data, respectively. D and F: Root mean squared error and standard deviation of estimated SIF_{760} and SIF_{687}, respectively, for the different deconvolution methods and PSFs. E: Bias of estimated SIF_{760}.

applied PSF.

4. Discussion and conclusion

All observations on the PSNR of synthetic data, as well as the behavior of real data are consistent with our considerations of the PSF calibration measurements, where the monochromator and misalignment introduce additional blur in the PSF itself. A too smooth PSF tells a deconvolution algorithm, that the input data to correct had been more strongly smoothed than it really has been smoothed. Thus the algorithm over-corrects the data, leading to unwanted amplitude amplifications in mid- and high frequent (in terms of Fourier domain) signal components. This is visible as strong noise amplification and ringing, i.e. strong over and undershoots as visible e.g. in the Wiener filtering result in Fig. 8**A–C** in the O_2A band from 765 nm to 767 nm.

The reconstruction using Wiener filtering together with a sharpened PSF, $\varphi_{\text{mean,Lucy}}$ or $\varphi_{\text{median,Lucy}}$, fulfills all quality criteria specified above, being consistent with our theoretical considerations and synthetic experiments. However, for signal reconstruction it is not forgiving, if the estimated PSF is somewhat too smooth. Therefore, in cases where the PSF might be too smooth and cannot be corrected reliably, 3 iterations of vanCittert's deconvolution is a better option, when reconstructing the hyperspectral signal is desired as final goal.

Surprisingly, for estimation of SIF_{760} Wiener filtering is forgiving a too smooth PSF, just leading to some underestimation of SIF instead of the overestimation common for all other algorithms. From this observation we conclude, that the strong over- and undershoots visible in the Wiener filtered signal (cmp. Fig. 7**A** and Fig. 8**A–C**) are mainly due to

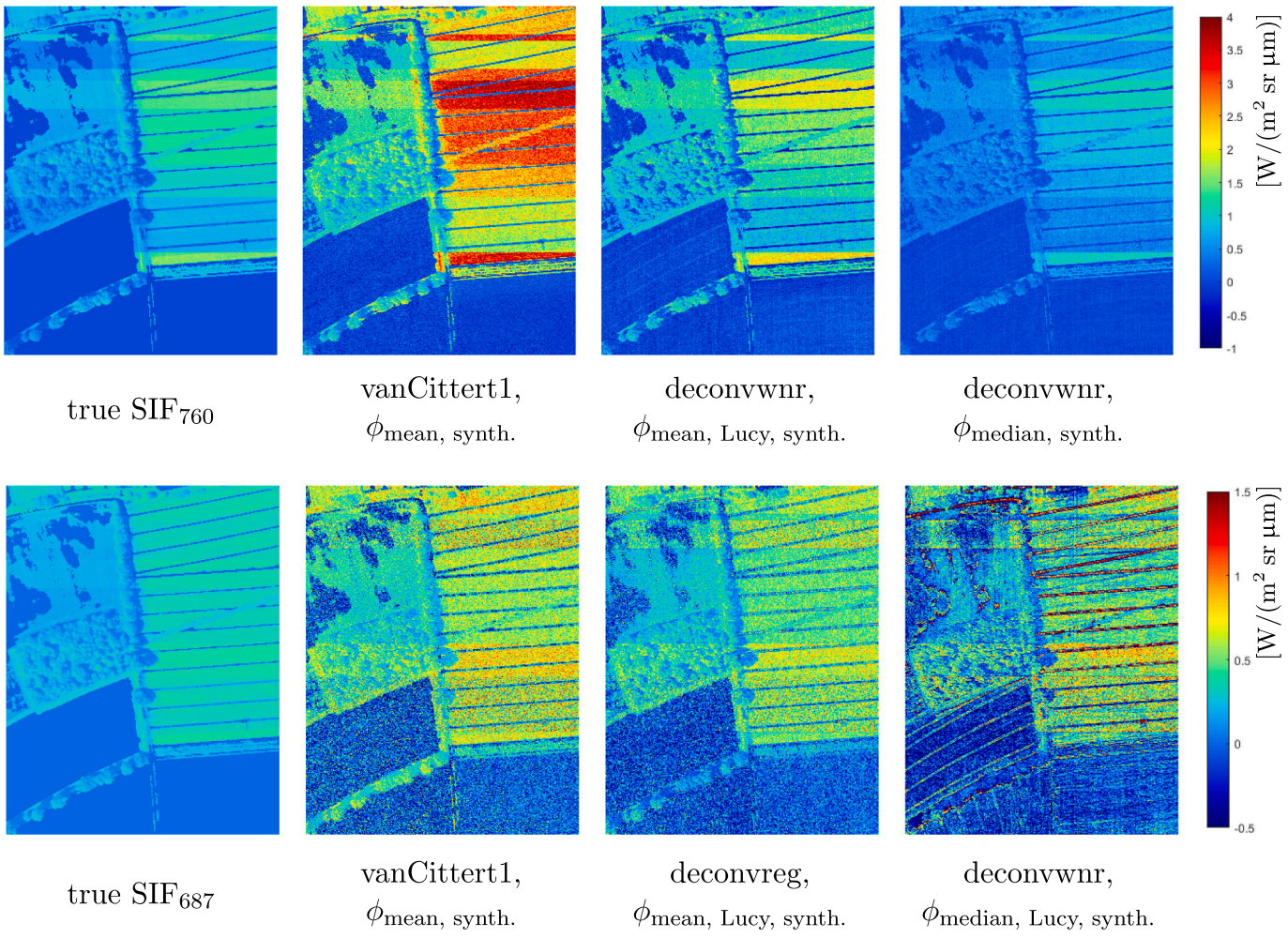

Fig. 11. Sun induced fluorescence maps. True SIF and results of three selected deconvolution algorithm - PSF combinations. Top: SIF_{760} maps scaled from -1 to 4 W/(m^2 sr μm). Bottom: SIF_{687} maps scaled from -0.5 to 1.5 W/(m^2 sr μm).

signal over-amplification and less due to too strongly amplified noise. Even though such an over-amplification of signal is strongly visible and indicates poor signal reconstruction, it seems to be of little effect to SIF_{760} retrieval using iFLD. The reduction of the smoothing effect of the PSF, however, seems crucial to SIF_{760} retrieval as can be concluded from Fig. 10**E**, where stronger correction (i.e. results for Wiener filtering with $\varphi_{mean,synth.}$ and $\varphi_{median,synth.}$ compared to $\varphi_{mean,Lucy,synth.}$ and $\varphi_{median,Lucy,synth.}$) lead to lower mean SIF_{760} values.

For the estimation of SIF_{687} we did not find a well-performing configuration where we can give a reliable recommendation. We speculate that the unstable behavior could be due to the coupling of the high signal O_2A band and low signal O_2B band in the PSNR-optimized deconvolution methods leading to relatively high errors in low signal regions. Coupling can be due to parameter settings (e.g. number of iterations, mean noise level, averaging of the PSF) or due to the application of Fourier transform in Wiener filtering, deconvreg and the Lucy-Richardson method. Coupling signal part of different amplitudes can have this unwanted effect, as absolute errors are small for low signals and large for large signals. Balancing the errors by applying a correction to both signal parts jointly, may then lead to a *relatively* large error in low signal parts. Further experiments would be needed to test this hypothesis and suggest an approach suitable for SIF_{687} retrieval.

For SIF estimation we therefore propose to use the O_2A band and classic Wiener filtering for deconvolution of FLUO data, combined with edge-tapering as border handling, our automated noise estimation in Fourier domain, and the novel mean- or median-aggregated and sharpened PSFs $\varphi_{median,Lucy}$ or $\varphi_{mean,Lucy}$. Which combination performs best depends on how close the available PSF is to the real one. For qualitative checks we propose to use the features described in Section 3.2 i.e. low ringing or overshoots, positivity, and closeness to the originally measured signal when re-convolving the deconvolved signal by the PSF.

We conclude that applying sharpening to a measured PSF is beneficial, when additional smoothing was introduced in the calibration measurements. Then such PSF sharpening allows to apply well-known strong deconvolution algorithms removing, or at least strongly reducing, blurring in spatio-spectral images introduced by the sensor's optics. This not only improves the spatio-spectral information itself, but can also have positive effects in terms of reduced uncertainty on subsequently derived quantities like SIF.

The main pitfalls of the selected method are that the initially measured PSF can be sharpened too little or too much. In the first case using a strong deconvolution algorithm like Wiener filtering may negatively affect signal quality, such that not applying any deconvolution may even be better (cmp. Fig. 6). However, this negative effect did not carry over to SIF_{760} estimates using iFLD, where using Wiener filtering always resulted in improvements compared to the baseline from Siegmann et al. (2019) (cmp. Fig. 10 **D, E**). Potential signal over- or undercorrections that might be introduced by our method are limited by two worst cases of (i) not sharpening the PSF, i.e. applying φ_{mean}, and (ii) sharpening the PSF to a delta peak resulting in no effect of the deconvolution, i.e. the case *unchanged* in our experiments. We therefore

conclude that process uncertainty due to potential signal under- or overcorrections is well controllable, and that the high benefit of reducing the mean squared error of SIF by a factor 3.8 outweighs this risk.

The iFLD method uses only two spectral lines in order to estimate SIF. For SIF retrieval methods using more information from the spectra, like e.g. the Spectral Fitting Method (Cogliati et al., 2019) using all the contiguous wavelengths over the spectral window from 680 nm to 780 nm, deteriorating the signal may carry over to SIF estimation. Same may be true when other target signals are of interest. However, we expect that when the PSF is sharpened adequately and the quality features from Section 3.2 (no over- or undershoots, reconvolved signal close to original) hold after applying deconvolution, that the improved signal quality carries over to most other subsequent measures derived from the signal. Clearly, to be certain, this needs to be tested for every derived quantity one may be interested in.

From this study, further desirable investigations become clear, which may be interesting for future research. The first is an adaptation of blind deconvolution to the scenario of highly peaked PSFs stemming from high-quality instruments. The tested blind deconvolution algorithm (MathWorks Inc., 2021) unfortunately had no update effect on the PSF, presumably because the PSF quality was high from the beginning. The second could be to look into deconvolution methods based on local Fourier transforms or wavelet-based reconstructions, which have been successfully used in other application scenarios. They would be beneficial in order to decouple the high signal O_2A band region from the low signal in the O_2B region. These regions additionally show clear differences in mean SNR, and somewhat different PSFs in the real calibration data, which should be appropriately considered in future research.

Declaration of Competing Interest

The authors declare that they have no known competing financial interests or personal relationships that could have appeared to influence the work reported in this paper.

Acknowledgements

The authors thank Stefan Kaft and Jose Moreno for fruitful discussion on the topic, and the anonymous reviewers for their helpful comments. This work has been partly funded by the Helmholtz AI funding line of the Helmholtz Association (HGF), Germany, via the FluoMap project. Support was provided by the SFB/TR 32 “Patterns in Soil-Vegetation-Atmosphere Systems: Monitoring, Modelling, and Data Assimilation”–subproject D2 (www.tr32.de), funded by the Deutsche Forschungsgemeinschaft (DFG). Airborne acquisition was financed by the European Space Agency (ESA) in the frame of the HyFLEX campaign (ESA contract no. 4000107143/12/NL/FF/If CCN3).

Appendix A. Supplementary data

Supplementary data to this article can be found online at https://doi.org/10.1016/j.rse.2021.112718.

References

Alonso, L., Gómez-Chova, L., Vila-Francés, J., Amorós-López, J., Guanter, L., Calpe, J., Moreno, J., 2008. Improved fraunhofer line discrimination method for vegetation fluorescence quantification. IEEE Geosci. Remote Sens. Lett. 5.

Barnes, R., Brown, S., Lykke, K., Guenther, B., Xiong, X., Butler, J., 2010. Comparison of two methodologies for calibrating satellite instruments in the visible and near infrared. Earth Obs. Mission. Sens. Dev. Implement. Charact. 7862.

Beirle, S., Lampel, J., Lerot, C., Sihler, H., Wagner, T., 2017. Parameterizing the instrumental spectral response function and its changes by a super-gaussian and its derivatives. Atmos. Meas. Tech. 10, 581–598. URL: www.atmos-meas-tech.net/10/581/2017/.

Berk, A., Cooley, T.W., Anderson, G.P., Acharya, P.K., Bernstein, L.S., Muratov, L., Lee, J., Fox, M.J., Adler-Golden, S.M., Chetwynd, J.H., Hoke, M.L., Lockwood, R.B., Gardner, J.A., Lewis, P.E., 2004. MODTRAN5: a reformulated atmospheric band model with auxiliary species and practical multiple scattering options. In: Comeron, A., Carleer, M.R., Picard, R.H., Sifakis, N.I. (Eds.), Remote Sensing of Clouds and the Atmosphere IX, volume 5571. International Society for Optics and Photonics, SPIE, pp. 78–85.

Biggs, D., 1997. Acceleration of iterative image restoration algorithms. Appl. Opt. 36, 1766–1775.

Cogliati, S., Celesti, M., Cesana, I., Miglietta, F., Genesio, L., Julitta, T., Schuettemeyer, D., Drusch, M., Rascher, U., Jurado, P., Colombo, R., 2019. A spectral fitting algorithm to retrieve the fluorescence spectrum from canopy radiance. Remote Sens. 11.

Cordts, M., Omran, M., Ramos, S., Rehfeld, T., Enzweiler, M., Benenson, R., Franke, U., Roth, S., Schiele, B., 2016. The cityscapes dataset for semantic urban scene understanding. In: Proc. of the IEEE Conference on Computer Vision and Pattern Recognition (CVPR), pp. 1–11.

Damm, A., Guanter, L., Laurent, V.C.E., Schaepman, M.E., Schickling, A., Rascher, U., 2014. Fld-based retrieval of sun-induced chlorophyll fluorescence from medium spectral resolution airborne spectroscopy data. Remote Sens. Environ. 147, 256–266.

Deneve, S., Latham, P.E., Pouget, A., 1999. Reading population codes: a neural implementation of ideal observers. Nature Am. Inc. 2, 740–745.

Deng, J., Dong, W., Socher, R., Li, L.-J., Li, K., Fei-Fei, L., 2009. Imagenet: a large-scale hierarchical image database. In: IEEE Conference on Computer Vision and Pattern Recognition, pp. 248–255.

Drusch, M., Moreno, J., Del Bello, U., Franco, R., Goulas, Y., Huth, A., Kraft, S., Middleton, E.M., Miglietta, F., Mohammed, G., Nedbal, L., Rascher, U., Schüttemeyer, D., Verhoef, W., 2017. The fluorescence explorer mission concept-esa's earth explorer 8. IEEE Trans. Geosci. Remote Sens. 55, 1273–1284.

European Space Agency & Forschungszentrum Jülich, 2016. Soxflex ii 2016 Campaign. https://doi.org/10.5270/ESA-24b3118.

Fish, D., Brinicombe, A., Pike, E., Walker, J., 1995. Blind deconvolution by means of the richardson-lucy algorithm. J. Opt. Soc. Am. A 12.

Gonzalez, R., Woods, R., 1992. Digital Image Processing. Addison-Wesley Publishing Company, Inc.

Guanter, L., Frankenberg, C., Dudhia, A., Lewis, P.E., Gómez-Dans, J., Kuze, A., Suto, H., Grainger, R.G., 2012. Retrieval and global assessment of terrestrial chlorophyll fluorescence from gosat space measurements. Remote Sens. Environ. 121, 236–251.

Hanisch, R., White, R., Gilliland, R., 1997. Deconvolution of hubble space telescope images and spectra. In: Jansson, P. (Ed.), Deconvolution of Images and Spectra. Academic Press, Boston, MA, pp. 310–356.

Heideman, M., Johnson, D., Burrus, C., 1984. Gauss and the history of the fast fourier transform. IEEE ASSP Mag. 1, 14–21. https://doi.org/10.1109/MASSP.1984.1162257.

Huang, C., Townshend, J.R., Liang, S., Kalluri, S.N., DeFries, R.S., 2002. Impact of sensor's point spread function on land cover characterization: assessment and deconvolution. Remote Sens. Environ. 80, 203–212.

Jähne, B., Haussecker, H., Geißler, P. (Eds.), 1999. Handbook of Computer Vision and Applications. Volume 1, Sensors and Imaging. Academic Press, San Diego.

Jähne, B., 2005. Digital Image Processing, 6 ed. Springer.

Jordan, C.F., 1969. Derivation of leaf-area index from quality of light on the forest floor. Ecology 50, 663–666.

Köhler, P., Frankenberg, C., Magney, T.S., Guanter, L., Joiner, J., Landgraf, J., 2018. Global retrievals of solar-induced chlorophyll fluorescence with tropomi: First results and intersensor comparison to oco-2. Geophys. Res. Lett. 45, 10456–10463.

Kruse, J., Rother, C., Schmidt, U., 2017. Learning to push the limits of efficient fft-based image deconvolution. In: The IEEE International Conference on Computer Vision (ICCV), pp. 4586–4594.

Levin, A., Weiss, Y., Durand, F., Freeman, W., 2009. Understanding and evaluating blind deconvolution algorithms. In: Proceedings of the IEEE Computer Society Conference on Computer Vision and Pattern Recognition, Miami, Florida, pp. 1964–1971.

Liu, X., Tanaka, M., Okutomi, M., 2013. Single-image noise level estimation for blind denoising. Trans. Img. Proc. 22, 5226–5237. https://doi.org/10.1109/TIP.2013.2283400.

Lucy, L., 1974. An iterative technique for the rectification of observed distributions. Astro. J. 79, 745–754. https://doi.org/10.1086/111605.

MathWorks, Inc., 2021. Edgetaper, https://de.mathworks.com/help/images/ref/edgetaper.html, accessed July 20, 2021.

MathWorks, Inc., 2021. Deconvblind, https://de.mathworks.com/help/images/ref/deconvblind.html, accessed July 20, 2021.

MathWorks, Inc., 2021. Deconvreg, https://de.mathworks.com/help/images/ref/deconvreg.html, accessed July 20, 2021.

MathWorks, Inc., 1994-2020. Matlab image processing toolbox.

McGillem, C., Anuta, P., Malaret, E., Yu, K.B., 1983. Estimation of a Remote Sensing System Point-Spread Function from Measured Imagery. Technical Report 062883, LARS Tech Report.

Meroni, M., Rossini, M., Guanter, L., Alonso, L., Rascher, U., Colombo, R., Moreno, J., 2009. Remote sensing of solar-induced chlorophyll fluorescence: Review of methods and applications. Remote Sens. Environ. 113, 2037–2051.

Mohammed, G.H., Colombo, R., Middleton, E.M., Rascher, U., van der Tol, C., Nedbal, L., Goulas, Y., Pérez-Priego, O., Damm, A., Meroni, M., Joiner, J., Cogliati, S., Verhoef, W., Malenovský, Z., Gastellu-Etchegorry, J.-P., Miller, J.R., Guanter, L., Moreno, J., Moya, I., Berry, J.A., Frankenberg, C., Zarco-Tejada, P.J., 2019. Remote sensing of solar-induced chlorophyll fluorescence (SIF) in vegetation: 50 years of progress. Remote Sens. Environ. 231, 111177.

Moya, I., Cerovic, Z.G., 2004. Remote Sensing of Chlorophyll Fluorescence: Instrumentation and Analysis, vol. 19. Springer Netherlands, Dordrecht, pp. 429–445.

Murchie, E.H., Kefauver, S., Araus, J.L., Muller, O., Rascher, U., Flood, P.J., Lawson, T., 2018. Measuring the dynamic photosynthome. Ann. Bot. 122, 207–220.
Paynter, I., Cook, B., Corp, L., Nagol, J., McCorkel, J., 2020. Spectrometer designed for remote sensing of solar induced fluorescence. Sensors 20, 4682. https://doi.org/10.3390/s20174682.
Peng, J., Liu, Q., Wang, L., Liu, Q., Fan, W., Lu, M., Wen, J., 2015. Characterizing the pixel footprint of satellite albedo products derived from modis reflectance in the heihe river basin, china. Remote Sens. 7, 6886–6907.
Plascyk, J., Gabriel, F., 1975. Fraunhofer line discriminator mkii: An airborne instrument for precise and standardized ecological luminescence measurement. IEEE Trans. Instru. Meas. 24, 306–313.
Quantum Design Europe, 2021. Czerny-Turner Monochromatoren. URL https://qd-europe.com/de/de/produkt/czerny-turner-monochromatoren/, accessed July 20, 2021.
Rascher, U., Alonso, L., Burkart, A., Cilia, C., Cogliati, S., Colombo, R., Damm, A., Drusch, M., Guanter, L., Hanus, J., Hyvärinen, T., Julitta, T., Jussila, J., Kataja, K., Kokkalis, P., Kraft, S., Kraska, T., Matveeva, M., Moreno, J., Muller, O., Panigada, C., Pikl, M., Pinto, F., Prey, L., Pude, R., Rossini, M., Schickling, A., Schurr, U., Schüttemeyer, D., Verrelst, J., Zemek, F., 2015. Sun-induced fluorescence - a new probe of photosynthesis: First maps from the imaging spectrometer hyplant. Glob. Change Biol. 21, 4673–4684.
Reeves, S.J., 2005. Fast image restoration without boundary artifacts. IEEE Trans. Image Process. 14, 1448–1453. https://doi.org/10.1109/TIP.2005.854474.
Ren, D., Zhang, K., Wang, Q., Hu, Q., Zuo, W., 2020. Neural blind deconvolution using deep priors. In: 2020 IEEE/CVF Conference on Computer Vision and Pattern Recognition (CVPR), pp. 3338–3347. https://doi.org/10.1109/CVPR42600.2020.00340.
Richardson, W., 1972. Bayesian-based iterative method of image restoration. JOSA 62, 55–59. https://doi.org/10.1364/JOSA.62.000055.
Sabater, N., Vicent, J., Alonso, L., Verrelst, J., Middleton, E., Porcar-Castell, A., Moreno, J., 2018. Compensation of oxygen transmittance effects for proximal sensing retrieval of canopy-leaving sun-induced chlorophyll fluorescence. Remote Sens. 10, 1551.
Siegmann, B., Alonso, L., Celesti, M., Cogliati, S., Colombo, R., Damm, A., Douglas, S., Guanter, L., Hanuš, J., Kataja, K., et al., 2019. The high-performance airborne imaging spectrometer hyplant-from raw images to top-of-canopy reflectance and fluorescence products: introduction of an automatized processing chain. Remote Sens. 11, 2760.
Simões, M., Almeida, L.B., Bioucas-Dias, J.M., Chanussot, J., 2016. A General Framework for Fast Image Deconvolution with Incomplete Observations. Applications to Unknown Boundaries, Inpainting, Superresolution, and Demosaicing. CoRR abs/1602.01410, URL: http://arxiv.org/abs/1602.01410.
Skilling, J., Gull, S., 1985. Algorithms and Applications, vol. 14. Springer, Dordrecht, pp. 83–132. See p.110 for edge tapering.
SPECIM, 2021. Datasheet Aisaibis: Measure Fluorescence from Air. https://www.specim.fi/wp-content/uploads/2020/03/AisaIBIS-ver1-2017.pdf, URL: https://www.specim.fi/products/aisaibis/, accessed July 20, 2021.
Thu, Q.H., Ghanbari, M., 2008. Scope of validity of PSNR in image/video quality assessment. Electron. Lett. 44, 800–801. https://doi.org/10.1049/el:20080522.
Tol, C., Verhoef, W., Timmermans, J., Verhoef, A., Su, B., 2009. An integrated model of soil-canopy spectral radiance observations, photosynthesis, fluorescence, temperature and energy balance. Biogeosci. Discuss. 6, 6025–6075.
van der Walt, S., Schönberger, J., Nunez-Iglesias, J., Boulogne, F., Warner, J., Yager, N., Gouillart, E., Yu, T., 2014. the scikit-image contributors, scikit-image: image processing in Python. PeerJ 2, e453. https://doi.org/10.7717/peerj.453.
Waldner, F., Duveiller, G., Defourny, P., 2018. Local adjustments of image spatial resolution to optimize large-area mapping in the era of big data. Int. J. Appl. Earth Observ. Geoinf. 73, 374–385.
Wang, Z., Wang, Z., Li, Q., Bilen, H., 2019. Image Deconvolution with Deep Image and Kernel Priors. In: 2019 IEEE/CVF International Conference on Computer Vision Workshop (ICCVW). IEEE Computer Society, Los Alamitos, CA, USA, pp. 980–989. https://doi.org/10.1109/ICCVW.2019.00127.
Wang, Q., Tang, Y., Atkinson, P.M., 2020a. The effect of the point spread function on downscaling continua. ISPRS J. Photogram. Rem. Sens. 168, 251–267.
Wang, Q., Zhang, C., Tong, X., Atkinson, P., 2020b. General solution to reduce the point spread function effect in subpixel mapping. Remote Sens. Environ. 251.
Wiener, N., 1942. The Interpolation, Extrapolation and Smoothing of Stationary Time Series. MIT. Technical Report.